Article

Immunity

Targeted Complement Inhibition at Synapses Prevents Microglial Synaptic Engulfment and Synapse Loss in Demyelinating Disease

Graphical Abstract

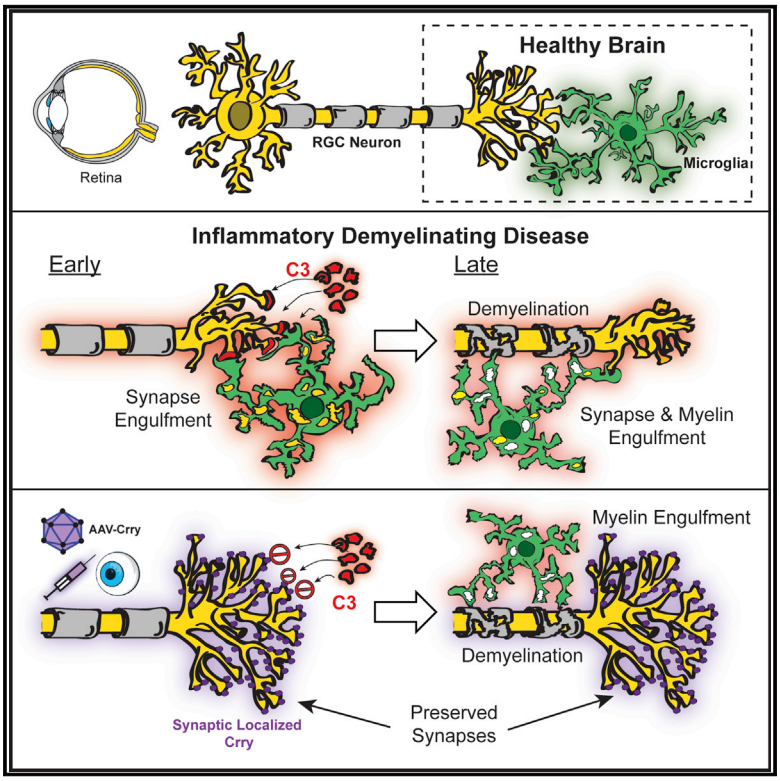

Highlights

- Microglia engulf and eliminate synapses in the visual thalamus of MS patients
- MS-relevant animal models show synapse engulfment and loss occur early in disease
- Complement C3, but not C1q, localizes to synapses in demyelinating disease
- AAV-Crry inhibits C3 and microglia-mediated synapse loss and preserves function

Authors

Sebastian Werneburg, Jonathan Jung, Rejani B. Kunjamma, ..., Brian Popko, Daniel S. Reich, Dorothy P. Schafer

Correspondence

dorothy.schafer@umassmed.edu

In Brief

The mechanisms underlying synaptic changes in multiple sclerosis (MS) remain unclear. Werneburg et al. identify microglia-mediated synapse engulfment and synapse loss in MS patients and multiple MS-relevant animal models. Synapse loss can occur early and prior to other MS-relevant pathology and is associated with synapse-localized complement C3. An AAV approach to inhibit C3 protects synapses and preserves circuit function.

Werneburg et al., 2020, Immunity *52*, 167–182
January 14, 2020
https://doi.org/10.1016/j.immuni.2019.12.004

CellPress

Immunity
Article

Targeted Complement Inhibition at Synapses Prevents Microglial Synaptic Engulfment and Synapse Loss in Demyelinating Disease

Sebastian Werneburg,[1] Jonathan Jung,[1] Rejani B. Kunjamma,[2] Seung-Kwon Ha,[3] Nicholas J. Luciano,[3] Cory M. Willis,[4] Guangping Gao,[5,6,7] Natalia P. Biscola,[8] Leif.A. Havton,[8,9] Stephen J. Crocker,[4] Brian Popko,[2] Daniel S. Reich,[3] and Dorothy P. Schafer[1,10,*]

[1]Department of Neurobiology, Brudnik Neuropsychiatric Research Institute, University of Massachusetts Medical School, Worcester, MA 01605, USA
[2]Department of Neurology, University of Chicago, Chicago, IL 60637, USA
[3]Translational Neuroradiology Section, National Institute of Neurological Disorders and Stroke, National Institutes of Health, Bethesda, MD 20892, USA
[4]Department of Neuroscience, University of Connecticut School of Medicine, Farmington, CT 06032, USA
[5]Horae Gene Therapy Center, University of Massachusetts Medical School, Worcester, MA 01605, USA
[6]Li Weibo Institute for Rare Diseases Research, University of Massachusetts Medical School, Worcester, MA 01605, USA
[7]Department of Microbiologic and Physiological Systems, University of Massachusetts Medical School, Worcester, MA 01605, USA
[8]Department of Neurology, David Geffen School of Medicine at UCLA, Los Angeles, CA 90095, USA
[9]Department of Neurobiology, David Geffen School of Medicine at UCLA, Los Angeles, CA 90095, USA
[10]Lead Contact
*Correspondence: dorothy.schafer@umassmed.edu
https://doi.org/10.1016/j.immuni.2019.12.004

SUMMARY

Multiple sclerosis (MS) is a demyelinating, autoimmune disease of the central nervous system. While work has focused on myelin and axon loss in MS, less is known about mechanisms underlying synaptic changes. Using postmortem human MS tissue, a preclinical nonhuman primate model of MS, and two rodent models of demyelinating disease, we investigated synapse changes in the visual system. Similar to other neurodegenerative diseases, microglial synaptic engulfment and profound synapse loss were observed. In mice, synapse loss occurred independently of local demyelination and neuronal degeneration but coincided with gliosis and increased complement component C3, but not C1q, at synapses. Viral overexpression of the complement inhibitor Crry at C3-bound synapses decreased microglial engulfment of synapses and protected visual function. These results indicate that microglia eliminate synapses through the alternative complement cascade in demyelinating disease and identify a strategy to prevent synapse loss that may be broadly applicable to other neurodegenerative diseases.

INTRODUCTION

Multiple sclerosis (MS) is a neurological disease of the central nervous system (CNS) affecting more than 2 million people worldwide (GBD 2016 Multiple Sclerosis Collaborators, 2019). The disease is typically characterized by recurrent episodes of inflammatory demyelination with a relapsing-remitting course, which can be accompanied by neurodegeneration (Reich et al., 2018; Amato et al., 2010). A subset of patients initially present with or develop a progressive, chronic neurodegenerative disease with significant synapse loss and CNS atrophy, termed progressive MS (Mahad et al., 2015). Current FDA and EMA-approved disease-modifying therapies, which inhibit peripheral immune attack of the CNS in MS, are increasingly effective at reducing episodes of inflammatory demyelination and neurological disability (Mahad et al., 2015; Weideman et al., 2017). However, the neurodegenerative process, particularly for patients with progressive MS, has proven more challenging to decelerate (Ciotti and Cross, 2018). Similar to other neurodegenerative diseases, there is no clear mechanistic understanding of why some patients develop profound degeneration and disability. Therefore, studying neurodegeneration in MS may offer an opportunity to capture early phases of the degenerative process, which may be broadly applicable to other CNS diseases and could lead to therapeutic strategies to meet an urgent clinical need.

Synapse loss is an early and likely key feature underlying circuit dysfunction in many neurodegenerative diseases, including Alzheimer's disease and other related dementias (Selkoe et al., 2008; Mucke and Selkoe, 2012; Selkoe, 2002; Milnerwood and Raymond, 2010; Yoshiyama et al., 2007; Coleman et al., 2004; Forner et al., 2017; Tyebji and Hannan, 2017; Henstridge et al., 2016). However, compared to other diseases, far less is known regarding how synaptic connections are affected in MS. The vast majority of research aimed at treating neurodegenerative aspects of MS focus on mechanisms of de- and remyelination, as well as axon de- and regeneration (Lassmann, 2010, 2018; Mahad et al., 2015; Dutta and Trapp, 2011; Reich et al., 2018). From the few studies assessing synaptic changes in postmortem MS tissue, synapse loss is observed in the hippocampus and normal-appearing gray matter in the cortex (Dutta et al., 2011;

Jürgens et al., 2016). Similar results are found in rodent models of demyelinating disease. For example, in a cuprizone model of demyelination, a significant decrease in excitatory synapses is observed in the visual thalamus concomitant with reactive gliosis and subcortical demyelination (Araújo et al., 2017). In another study, experimental autoimmune encephalomyelitis (EAE)-induced demyelination in mice results in a ~28% decrease in post-synaptic density protein 95 (PSD-95)-positive postsynaptic densities in the hippocampus, which is observed in the absence of hippocampal demyelination but in the presence of reactive microglia (Bellizzi et al., 2016). A common feature in all these studies is reactive gliosis, including pronounced increases in inflammatory microglia, a resident CNS macrophage (Lassmann, 2010, 2018; Mahad et al., 2015; Voet et al., 2019). However, it remains unclear if and how these inflammatory glial cells could modulate synaptic connectivity in demyelinating disease.

Microglia have recently been identified as key regulators of synaptic connectivity in the healthy and diseased brain. During development, microglia regulate synaptic pruning by engulfing and removing a subset of less-active synapses (Hong et al., 2016b). One key mechanism is classical complement cascade-dependent phagocytic signaling (Stevens et al., 2007; Schafer et al., 2012). In the peripheral immune system, components of the classical complement cascade, C1q and C3, bind the surface of invading pathogens, cellular debris, etc., leading to clearance by professional phagocytes that express complement receptors (CRs) (Carroll, 1998; Morgan and Kavanagh, 2018; Lambris and Tsokos, 1986; Reis et al., 2019). Similarly, in the developing rodent visual thalamus, C1q and C3 localize to synapses (Stevens et al., 2007). Microglia expressing CR3, a C3 receptor, then engulf these complement-associated synapses. Mice deficient in either CR3 expressed by microglia, C3, or C1q have a ~50% decrease in their ability to engulf and remove synapses (Schafer et al., 2012; Bialas and Stevens, 2013). Classical complement cascade-mediated phagocytic signaling is also aberrantly upregulated in mouse models of Alzheimer's disease, frontotemporal dementia, and West Nile virus infection, leading to synapse loss (Hong et al., 2016a; Vasek et al., 2016; Lui et al., 2016). In MS patients, complement proteins are elevated systemically and in the CNS (Aeinehband et al., 2015; Ingram et al., 2009, 2012; Watkins et al., 2016), and recent work suggests that C1q and C3 colocalize with synaptic proteins in postmortem MS brains (Michailidou et al., 2015). However, it remains elusive if complement and/or microglia are necessary for synaptic changes in MS.

In the current study, we use the retinogeniculate system to study synaptic changes in demyelinating disease. The retinogeniculate system is comprised of retinal ganglion cells (RGCs), which are neurons in the retina that extend their axons via the optic nerve and tract and synapse onto relay neurons within the lateral geniculate nucleus (LGN) of the thalamus. This circuit was chosen because even subtle synaptic changes are readily detected by immunohistochemical methods (Schafer et al., 2012, 2016; Hong et al., 2014). In addition, the anterior visual pathway is commonly affected in MS, with upward of 50% of patients experiencing inflammation of the optic nerve (i.e., optic neuritis) and prolonged visual dysfunction (Toosy et al., 2014; Reich et al., 2018). Using postmortem human MS tissue, a preclinical nonhuman primate model of MS, and two different rodent models of demyelinating disease, we investigated early synapse changes in the retinogeniculate system. Profound synapse loss and engulfment of synaptic material by microglia, but not astrocytes, were detected in the LGN from human MS tissue and in all MS-relevant animal models. In rodents and nonhuman primates, synapse loss in demyelinating disease occurred independent of neuronal cell death or axon degeneration and, in some cases, prior to significant demyelination. In all species, synapse loss occurred concomitant with reactive gliosis. To identify a molecular mechanism underlying this synapse loss, we focused on the complement cascade and provide evidence for activation of the alternative, but not the classical, complement cascade at synapses in demyelinating disease. We then used an adeno-associated viral (AAV) approach to overexpress the C3 inhibitor Crry at sites of synaptic C3 activation in the retinogeniculate circuit and demonstrated robust protection from synapse engulfment by microglia and synapse loss. The rescue of structural synapses with this AAV approach was specific to the retinogeniculate circuit and restored function as assessed by visual acuity. Together, our data provide evidence that local inflammatory microglia and the alternative complement cascade mediate synapse loss and functional decline in demyelinating disease. With our data demonstrating that targeted inhibition of activated C3 protects synapses, we further uncover a strategy to prevent synapse loss at specific synapses and preserve circuit function during neurodegeneration.

RESULTS

MS Patients and a Preclinical Marmoset EAE Model Display Profound Synapse Loss and Microglial Engulfment of Presynaptic Terminals

To first interrogate retinogeniculate synaptic changes that are clinically relevant to MS, we assessed synaptic connectivity in postmortem LGN from MS and control patients without neurological disease (Figures S1A–S1F; Table S1). Using anti-vesicular glutamate transporter 2 (VGluT2) immunostaining, a marker specific to retinogeniculate presynaptic inputs, and confocal imaging, we observed a significant decrease in retinogeniculate presynaptic terminals within the LGN of MS patients compared to controls (Figure 1A). Colabeling with the microglia and macrophage marker Iba1 and 3D surface rendering further revealed that significant amounts of VGluT2^{+}-terminals were engulfed within Iba1^{+}-cells with morphological characteristics of microglia versus peripheral macrophages (Figure 1B). These results are consistent with previous work showing significant degeneration of the thalamus and deep gray matter early in the disease course of MS, which accurately predicts subsequent disease severity (Eshaghi et al., 2018; Zivadinov et al., 2013). This is also in line with studies showing decreases in presynaptic inputs in the hippocampus and cortex of postmortem MS tissue (Dutta et al., 2011; Jürgens et al., 2016) and studies demonstrating that microglia engulf and eliminate synaptic components in other models of neurodegenerative disease (Hong et al., 2016a; Paolicelli et al., 2017; Lui et al., 2016; Vasek et al., 2016).

We next sought to corroborate these findings in a preclinical nonhuman primate model of MS, EAE in common marmosets induced by immunization with human white matter homogenate (Lee et al., 2018). This model is particularly powerful as it has many of the pathological features present in human MS (Absinta

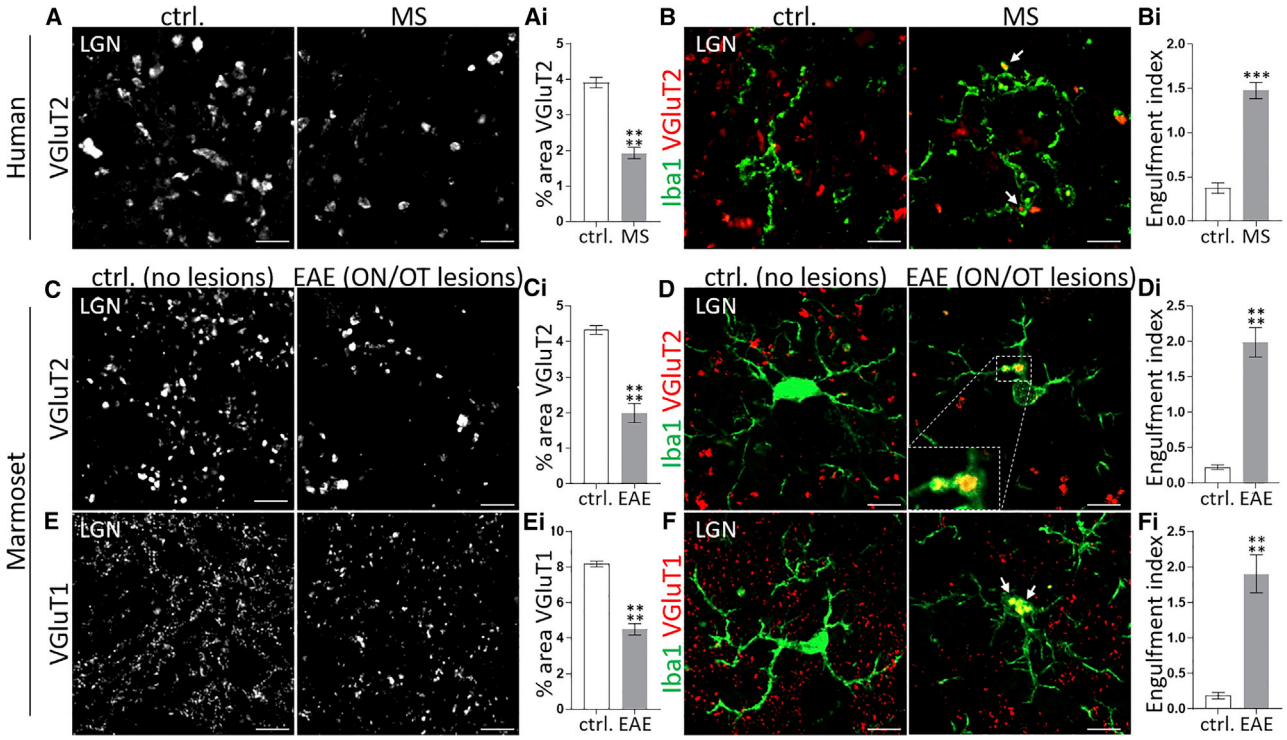

Figure 1. Synapse Loss and Engulfment of Presynaptic Terminals Occurs in the LGN of MS Patients and in a Preclinical Marmoset EAE Model

(A and B) Coronal sections of the LGN from human controls (ctrl.) without neurological disease and from MS cases are shown. (A and Ai) Quantification of VGluT2$^+$-retinogeniculate presynaptic input density (red) and (B and Bi) engulfment of VGluT2$^+$-presynaptic inputs within (arrows) Iba1$^+$-cells (green). (Ai) n = 5 human subjects per condition. (Bi) n = 3 ctrl. and 5 MS subjects. Scale bars, 10 μm.

(C–F) Representative images of the LGN from non-EAE or EAE animals with no detectable lesions (control, no lesions) and marmosets that developed EAE with demyelinating lesions in the optic nerve and tract (EAE with ON/OT lesions). (Ci) Quantification of VGluT2$^+$-input density (red) and (Di) engulfment of VGluT2$^+$-presynaptic RGC inputs within Iba1$^+$ cells (green) in the LGN from marmosets that developed ON and OT lesions following EAE compared to controls. (D) Inset shows phagocytic cups within Iba1$^+$-cell (green), containing VGluT2$^+$-retinogeniculate synaptic material (red). (E and F) Immunostaining and quantification of VGluT1$^+$-corticothalamic presynaptic inputs (E) density and (F) engulfment within Iba1$^+$-cells (arrows denote engulfed VGluT1$^+$-corticothalamic inputs). n = 6 marmosets per condition from two experiments. Scale bars, 10 μm.

Data represent mean ± SEM; significant differences with ***p < 0.001, ****p < 0.0001; t test. See also Figure S1 and Tables S1 and S2.

et al., 2016). Similar to MS patient LGN, we found a ~2-fold reduction in the density of retinogeniculate terminals and an increased localization of VGluT2 within Iba1$^+$-cells (Figures 1C and 1D) in the LGN from animals that developed EAE with demyelinating lesions in the optic nerve and tract (Figures S1G-S1K; Table S2). This contrasts with either EAE or non-EAE animals with no detectable lesions in the optic nerve and tract (Table S2), which were used as controls. Many of the engulfed VGluT2$^+$-retinogeniculate terminals were detected within microglial phagocytic cups, which were not present in Iba1$^+$cells from control animals (Figure 1D). To determine if loss of presynaptic inputs and engulfment by Iba1$^+$-cells is specific to retinogeniculate terminals or if synaptic connectivity within the LGN is affected more broadly, we assessed the density of corticothalamic inputs by immunostaining against VGluT1 in marmosets. Like retinogeniculate terminals, we also found a significant decrease in the density of VGluT1$^+$-corticothalamic inputs in the LGN and detected significant amounts of VGluT1 within Iba1$^+$-cells in marmosets with lesions in the optic nerve and tract following EAE (Figures 1E and 1F). These data provide evidence that microglia engulf and eliminate presynaptic inputs within the retinogeniculate circuit in demyelinating disease.

Synapse Loss Occurs in Two Independent Mouse Models of Demyelinating Disease

Retinogeniculate synapse loss in human and marmoset raised the following questions: (1) is synapse loss a separable feature of disease or secondary to other pathologies, and (2) what mechanism underlies synapse loss? We turned to mouse models to gain a deeper mechanistic understanding and address these questions. We assessed two distinct mouse models: a model of inflammatory demyelination and a model of primary demyelination. Inflammatory demyelination was induced using the $MOG_{35–55}$ C57Bl6/J mouse EAE model (Crocker et al., 2006). We assessed synapse density at the onset of clinical symptoms (average scores: 1.35 ± 0.35 at 10.8 ± 0.4 days post induction; Figure 2A) and made all comparisons to complete Freund's adjuvant (CFA)-treated controls. The other model we tested was the *Plp1-CreER^T;ROSA26-EGFP-DTA* (diphtheria toxin A [DTA]) mouse model of primary demyelination (Traka et al., 2010, 2016). In this model, 5- to 7-week-old DTA and control (ROSA26-EGFP-DTA) mice receive tamoxifen injections. In DTA mice, this induces the expression of DTA in mature oligodendrocytes, which results in demyelination within several weeks post injection (Figure 2D). For consistency, we performed

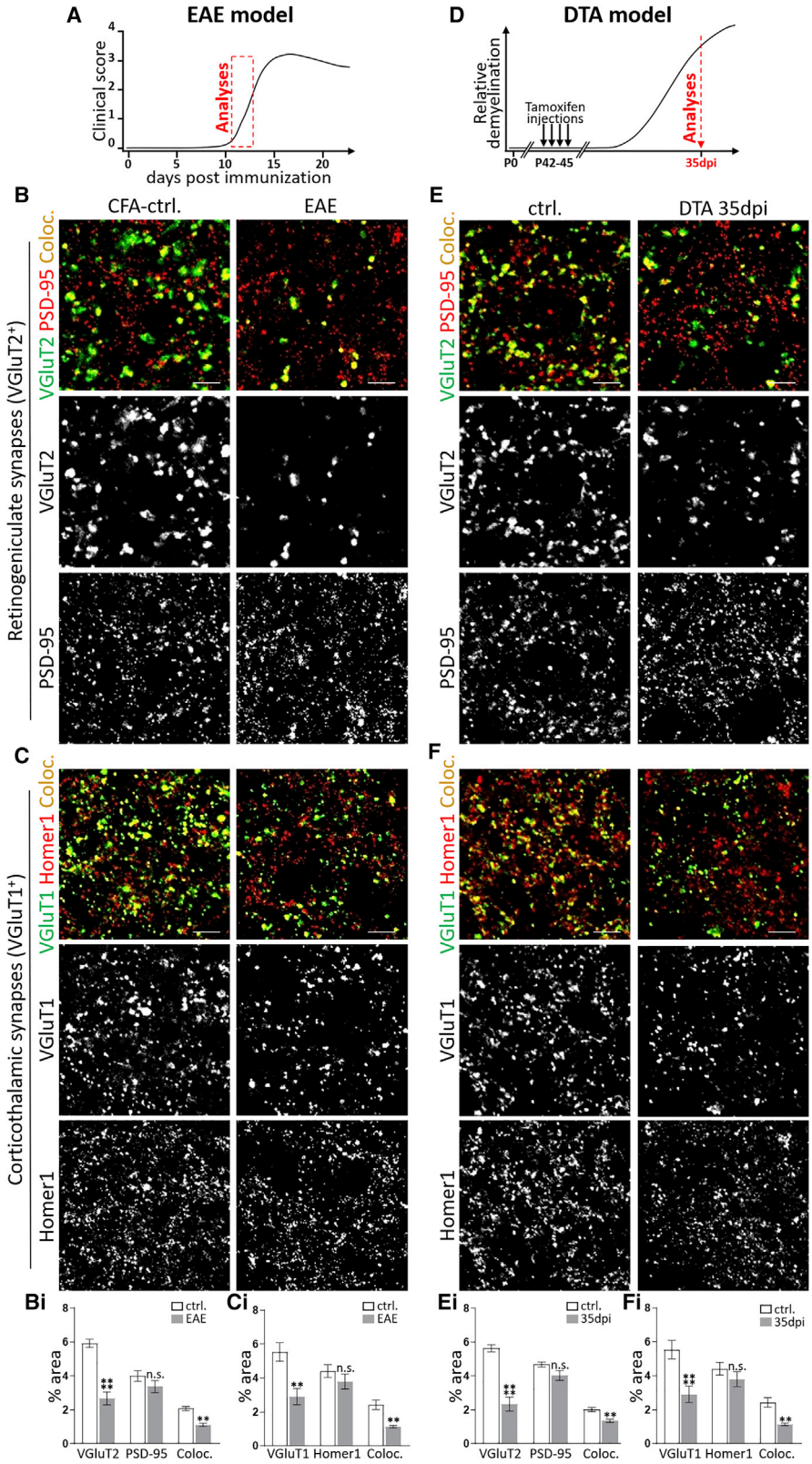

Figure 2. Synapse Loss Is a Common Feature in the Retinogeniculate Circuit of Multiple MS-relevant Mouse Models

(A) Schematic of the course of clinical symptoms in EAE of C57Bl6/J WT mice. Mice were analyzed at the onset of moderate clinical symptoms, typically observed between days 10 and 12 post immunization.

(legend continued on next page)

the bulk of our analyses in male mice. Also, in humans, while males are less prone to MS compared to females, they tend to develop more aggressive forms of the disease with more disability (Bove et al., 2012; Gholipour et al., 2011; Confavreux et al., 2000). Therefore, analysis of males is highly relevant for studying neurodegeneration related to MS.

Like human and marmoset data (Figure 1), we detected a significant, >50% reduction in VGluT2$^+$- and VGluT1$^+$-presynaptic inputs within the LGN at earlier stages of mouse EAE (Figures 2B and 2C) and during demyelination at 35 days post injection (dpi) in the DTA model (Figures 2E and 2F). This was accompanied by a pronounced reduction in the density of structural synapses (colocalized presynaptic VGluT2 or VGluT1 with postsynaptic PSD-95 or Homer1). However, this synapse loss was mainly attributed to a presynaptic effect in both models, as the densities of postsynaptic PSD-95 and Homer1 were relatively unaltered (Figures 2Bi, 2Ci, 2Ei, and 2Fi). These data are consistent with previously published work demonstrating preferential loss of presynaptic elements in the retinogeniculate system (Schafer et al., 2012, 2016). Note that in EAE, similar synapse loss was observed in female mice (Figures S4A and S4C). However, these effects were less robust compared to male mice, which could be one explanation underlying the more aggressive disease in human male MS patients. Taken together, these results are consistent with retinogeniculate synapse loss as a common feature in human MS and across nonhuman primate and multiple mouse models of disease.

Synapse Loss Can Occur Independent of Significant Demyelination, Cell Death, or Axon Degeneration

In the human MS cases, patients have had protracted disease with demyelination (Figures S1A and S1B), and many patients had a history of optic neuritis (Table S1). Likewise, in the marmoset EAE and mouse DTA models, there were indications of demyelination in the LGN and optic tract (Figures S1G, S1H, S5A, and S5B; Table S2). Although there were some signs of apoptotic cells and mild axonal degeneration in the human LGN (Figures S1C–S1F), we found no indications of neuron or axonal loss in nonhuman primate and DTA mouse models (Figures S1I–S1K and S5C–S5G). These data raise the possibility that synaptic changes could be a separable, independent event in the degenerative process. This idea is supported by human imaging studies where thalamic degeneration is an accurate predictor of subsequent MS-related disability (Eshaghi et al., 2018; Zivadinov et al., 2013). To further test this possibility, we assessed demyelination, neuron cell loss, and axon degeneration in the mouse EAE model at the onset of clinical symptoms. While we observed significant increases in peripheral immune cells (Figures S2A and S2B), we detected no significant changes in the myelin sheath in the retinogeniculate circuit at early stages of EAE when we detected synapse loss (average clinical scores: 1.35 ± 0.35; Figures 3A–3C and S3A–S3F). These analyses included electron microscopy to measure G-ratios and myelin thickness in the optic nerve, assessment of nodes of Ranvier and paranodal junctions in the optic nerve by immunofluorescence microscopy (Wolswijk and Balesar, 2003; Howell et al., 2006), and assessment of immunofluorescence intensity for myelin proteins (MOG, MBP, and MAG) in the optic tract, the LGN, and optic nerve in EAE compared to CFA controls. Similar to marmoset EAE and DTA models, there were also no significant changes in the density of NeuN$^+$ neurons or neurofilament$^+$ axons and no significant increases in the number of cleaved caspase 3$^+$-apoptotic cells or amyloid precursor protein (APP) accumulations in axons within the retinogeniculate circuit at these early phases of mouse EAE (Figures 3D–3G and S3G–S3K). These results demonstrate that synapse loss can occur prior to neuronal degeneration in multiple models and, in the case of mouse EAE, prior to myelin pathology but in the presence of local inflammation.

Reactive Microglia, but Not Astrocytes, Engulf Synapses in MS-Relevant Animal Models

Given our initial data demonstrating microglial engulfment of synapses in human MS and marmoset EAE LGN, we hypothesized that reactive glia were responsible for the loss of synapses in demyelinating disease. Indeed, a common pathological feature across models was reactive gliosis (Figures S2C–S2E and S5J–S5M) and the presence of infiltrating peripheral immune cells, albeit less severe in the DTA model (Figure S2A, S2B, S5H, and S5I). The reactive gliosis in mouse models included microglia with a neurodegenerative phenotype (Krasemann et al., 2017; Keren-Shaul et al., 2017), indicated by reduced P2RY12, a marker of homeostatic microglia, and increased Clec7a, a neurodegeneration-associated marker. To further examine whether local inflammatory gliosis was a contributing factor to early synapse loss, we tested whether reactive microglia engulfed presynaptic terminals in the mouse EAE and DTA models. We labeled microglia with anti-P2RY12, which distinguishes resident microglia from peripheral infiltrating macrophages (Butovsky et al., 2014; Jordão et al., 2019), and microglial lysosomes with anti-CD68 to assess engulfed presynaptic terminals using confocal imaging and 3D surface rendering. Like with data from humans and marmosets (Figure 1), we found a ~10-fold increase in the engulfment of VGluT2$^+$- and VGluT1$^+$-presynaptic inputs within microglial lysosomes in the LGN in male EAE and DTA mice (Figures 4A, 4B, 4D, and 4E) compared to controls. Note that while overall P2RY12 was reduced, it was still detectable, allowing us to distinguish microglia from peripheral myeloid cells. Synaptic

(B and C) Representative images of the LGN from CFA-control and EAE-induced mice immunostained against (B) presynaptic VGluT2 (green) and postsynaptic PSD-95 (red) or (C) presynaptic VGluT1 (green) and postsynaptic Homer1 (red). (Bi and Ci) Quantification of synaptic staining in (B) and (C). n = 4 mice per condition from one experiment.

(D) Schematic for tamoxifen-induced genetic depletion of mature oligodendrocytes in *Plp1-CreER^T;ROSA26-EGFP-DTA* (DTA) mice. Tamoxifen-injected ROSA26-EGFP-DTA mice were used as controls. The LGN of mice was analyzed at 35 dpi.

(E and F) Representative confocal images of the LGN from control and DTA mice immunostained against (E) presynaptic VGluT2 (green) and postsynaptic PSD-95 (red) or (F) presynaptic VGluT1 (green) and postsynaptic Homer1 (red). (Ei and Fi) Quantification of synaptic staining in (E) and (F). n = 5 ctrl. and 4 DTA mice from two experiments.

(B–F) Scale bars, 5 μm.

Data represent mean ± SEM; significant differences with **p < 0.01, ****p < 0.0001; t test. See also Figures S2, S3, and S5.

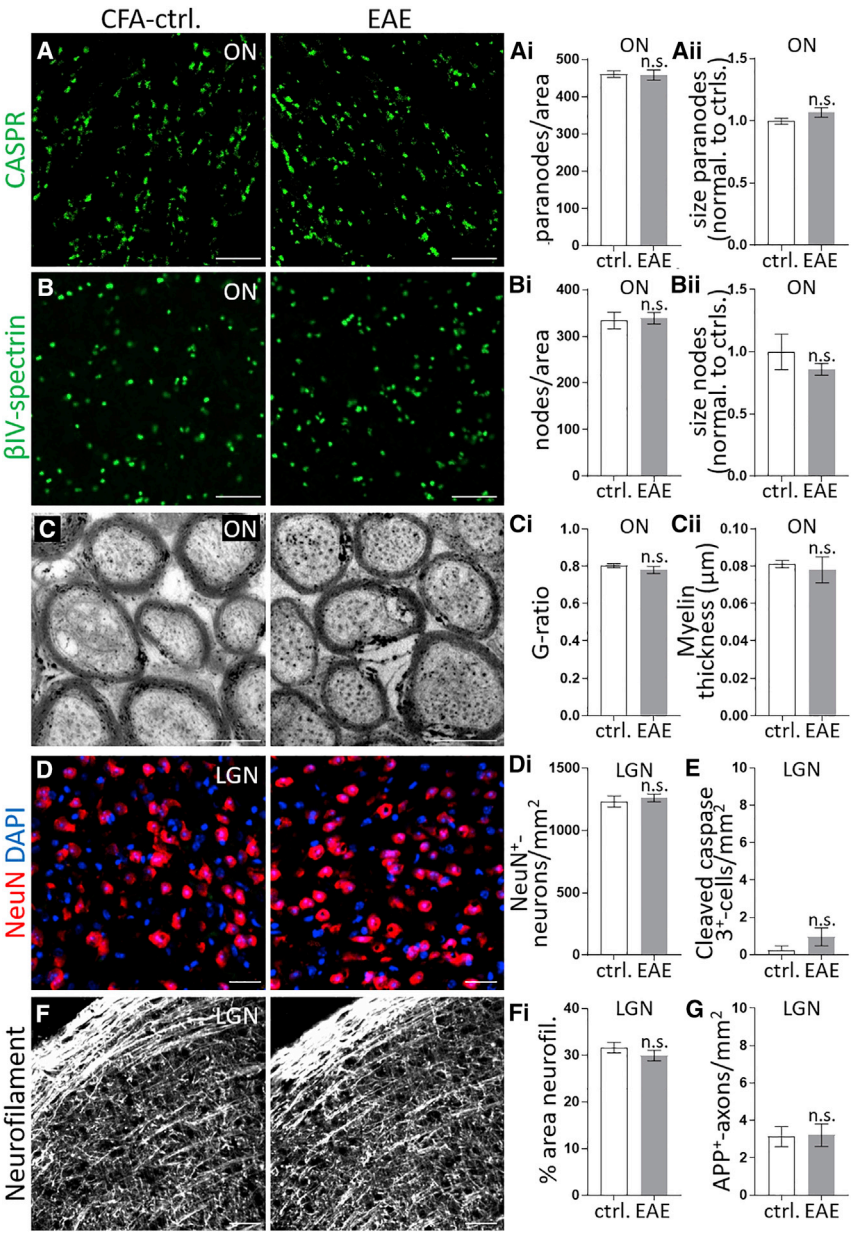

Figure 3. Synapse loss in the LGN can occur in the absence of significant demyelination, cell death, or axon degeneration at early stages of mouse EAE

(A, B, D–G) (A and B) Analysis of the optic nerve (ON) and (D–G) adjacent LGN sections of the same CFA-control and EAE-treated mice shown in Fig. 2. n = 4 mice per condition from one experiment.

(A and B) Representative images of (A) anti-CASPR-labeled paranodes and (B) anti-βIV-spectrin-labeled nodes of Ranvier and quantification of nodal and paranodal (Ai and Bi) density and (Aii and Bii) size (normalized to controls). (A and B) Scale bars, 10 μm.

(C) Ultrastructural analysis of the ON of an additional cohort of EAE mice at the onset of EAE (average: 12.2 ± 1.6 dpi) that displayed comparable average clinical score (1.2 ± 0.25) to the mice analyzed in Figure 2 and (A), (B), and (D)(F). Representative electron microscopy (EM) images of the optic nerve from EAE and CFA-ctrl. mice at 15,000× magnification. Scale bars, 0.5 μm. (Ci) G-ratio (ratio between the axon and fiber diameters) and (Cii) myelin thickness were quantified from EM images. n = 5 mice per condition from one experiment.

(D) Representative images of immunostaining in the LGN for the neuronal maker NeuN (red), with DAPI counterstain labeling all nuclei (blue) and quantification of the density of (Di) $NeuN^+$-neurons and (E) cleaved caspase 3^+-cells, a marker of cell death.

(F) Representative images of neurofilament (neurofil.)-labeled axons and quantification of (Fi) neurofilament$^+$-axon density and (G) APP, a marker of axonal degeneration, induction.

(D and F) Scale bars, 20 μm.

Data represent mean ± SEM; no significant differences (n.s.); t test. See also Figures S2 and S3.

engulfment by microglia was also detected in female EAE mice but, similar to synapse loss, was less pronounced compared to males (Figures S4B and S4D). There was no evidence for engulfment of postsynaptic compartments in EAE mice (Figure 4C). This latter finding is in line with other reports showing that microglia predominantly engulf presynaptic inputs (Schafer et al., 2012, 2014; Weinhard et al., 2018; Gunner et al., 2019) and our findings that the densities of postsynaptic compartments were relatively unaltered in EAE and DTA mice (Figure 2).

In addition to microglia, astrocytes engulf synaptic material during postnatal development of the visual system (Chung et al., 2013). To test if reactive astrocytes similarly engulf synaptic material in a demyelinating disease context, we stained astrocytes in the LGN with an antibody against ALDH1L1 and assessed engulfment of VGluT2 into $LAMP2^+$ lysosomes in the mouse EAE and DTA models. No engulfment of VGluT2 was detected within astrocytes in either model (Figures 4F and 4G). We found similar effects in the marmoset EAE model (Figure 4H). These data suggest that while astrocytes engulf synapses during developmental synaptic pruning, reactive astrocytes are not contributing to the engulfment of presynaptic terminals in demyelinating disease. This is consistent with recent work demonstrating that reactive astrocytes are less capable of phagocytosis (Liddelow et al., 2017). Together, these data demonstrate that reactive gliosis is a common feature across demyelinating disease, which can occur prior to significant demyelination in mouse EAE and in the absence of significant axonal or neuronal degeneration in all animal models tested. Our data further suggest that reactive microglia mediate synapse engulfment and elimination in demyelinating disease.

Complement Component C3, but Not C1q, Localizes to Synapses in Animal Models of MS

Previous work in mice has shown that microglial engulfment and elimination of synapses in development and in models of neurodegeneration is mediated by the classical complement cascade (Hong et al., 2016b). In this cascade, the initiating

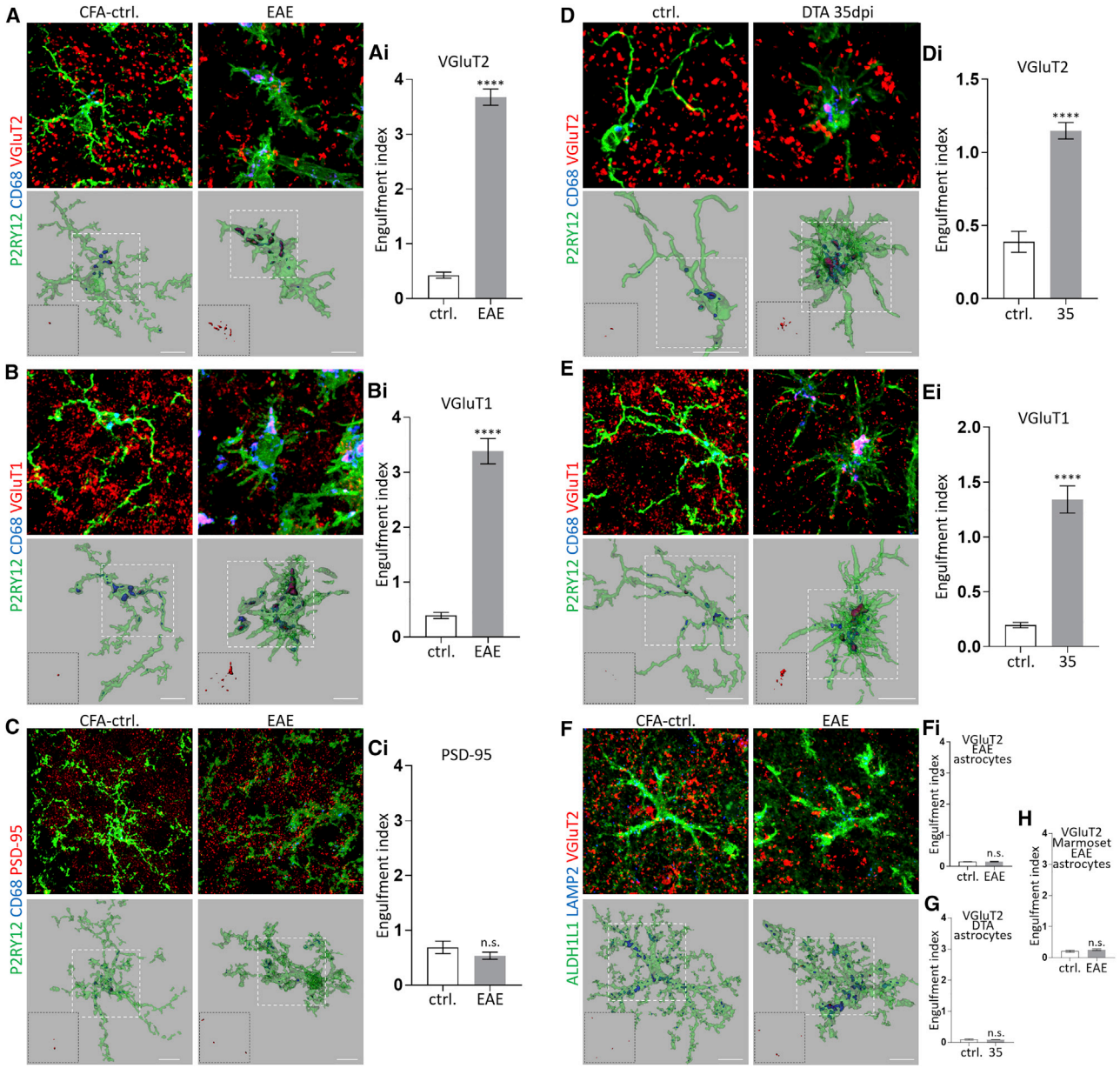

Figure 4. Microglia, but Not Astrocytes, Engulf Presynaptic Inputs in Multiple Models of Demyelinating Disease

Synapse engulfment was analyzed in the LGN from the same mouse EAE tissue (A–C and F; see also Figures 2, 3, S2, and S3) and the same mouse DTA tissue (D, E, and G; see also Figures 2 and S5) where synapse loss was observed.

(A–C) Representative immunofluorescence images and 3D surface rendering of P2RY12^{+}-microglia (green) containing engulfed (A) VGluT2^{+}-retinogeniculate inputs (red, inserts), (B) VGluT1^{+}-corticothalamic inputs (red, inserts), or PSD-95^{+}-postsynaptic compartments (red, inserts) within CD68-labeled microglial lysosomes (blue) in the EAE model. (Ai–Ci) Quantification of presynaptic inputs within microglial lysosomes in EAE versus CFA control mice.

(D and E) Representative confocal images and 3D rendering of P2RY12 (green), CD68 (blue) and (D) VGluT2 (red) or (E) VGluT1 (red) in the DTA model. (Di and Ei) Quantification of presynaptic inputs within microglial lysosomes in the DTA model.

(F) Representative images and 3D surface rendering of ALDH1L1^{+}-astrocytes (green) and VGluT2^{+}-retinogeniculate inputs (red, inserts) within LAMP2-labeled lysosomes (blue) in the LGN of EAE and CFA control mice. (Fi) Quantification of VGluT2 engulfment within lysosomes of reactive astrocytes in the EAE model.

(G and H) Quantification of VGluT2^{+}-retinogeniculate inputs within LAMP2^{+} lysosomes of ALDH1L1-labeled astrocytes in the (G) mouse DTA model and (H) marmoset EAE model.

(A–C, F) n = 4 mice per condition from one experiment, (D, E, G) n = 6 ctrls. and 5 DTA mice from two experiments, and (H) n = 6 marmosets per condition from two experiments. (A–F) Scale bars, 10 μm.

Data represent mean ± SEM; significant differences with ****$p < 0.0001$; t test. See also Figures S2, S3, and S5.

molecule C1q and downstream C3 localize to synapses, and microglia that express the receptor for C3 (CR3) engulf and eliminate synapses (Stevens et al., 2007; Schafer et al., 2012). These complement factors also increase in other CNS regions in EAE and MS patient tissue (Nataf et al., 2000; Ingram et al., 2012, 2014; Michailidou et al., 2015, 2017; Watkins et al., 2016), but it is unknown if complement mediates synapse loss in these contexts. We first assessed C1q and C3 protein in the retinogeniculate system in mouse and marmoset EAE. This analysis revealed a significant increase in C1q and C3 in the LGN in both species following EAE (Figure 5). However, despite increases in C1q throughout the LGN, it did not colocalize with presynaptic terminals (Figures 5A, 5B, 5E, and S4E). In contrast, complement factor C3 was colocalized with both presynaptic terminal markers and enrichment at synaptic compartments (Figures 5C, 5D, 5F, and S4F). The same observations were made in the mouse DTA model (Figures S5N and S5O). These data support a complement-dependent model by which microglia engulf and eliminate synapses. However, unlike developmental and other neurodegenerative disease contexts, synapse loss in demyelinating disease is independent of C1q localization to synapses. Instead, our data support the involvement of the alternative complement cascade, which bypasses C1q and works directly through synapse-localized activated C3, to mediate synapse loss.

AAV9-Mediated Expression of a C3 Inhibitor at Retinogeniculate Synapses

To test whether synapse-localized, activated C3 was inducing microglia-mediated synapse engulfment and elimination, we took a gene therapy approach. We used AAV9 to overexpress the complement inhibitor Crry, which restricts C3 activation and inhibits C3-mediated opsonization (Turnberg and Botto, 2003; Molina, 2002) in the retinogeniculate circuit (Figure 6A). To gain further specificity, we fused Crry to a domain of CR2, which is a receptor that binds activated C3. Following the sequence encoding the Crry-CR2-fusion protein was an autocleavage site and an EGFP sequence, which we used to identify transduced neurons and their projections. We termed this vector AAV-Crry. The Crry-CR2 fusion protein is targeted by the CR2 domain to sites of activated C3 deposition, where Crry then inhibits further C3 activation (Alawieh et al., 2015; Atkinson et al., 2005, 2006; Qiao et al., 2006; Alawieh and Tomlinson, 2016). For a control vector, we used an EGFP-encoding construct (AAV-EGFP). AAV9 viral vectors were then generated and validated in cultured neuro-2a (N2a) cells. 1 week after viral transduction, western blot analysis revealed robust expression of Crry and EGFP in transduced N2a cells (Figure 6B). Following initial validation, AAV-Crry or AAV-EGFPs were injected into the vitreous of both eyes of separate cohorts of 4-week-old wild-type (WT) mice to transduce RGCs. 28 days following AAV delivery, EAE was induced in these mice (Figure 6C). Mice were then analyzed at the onset of clinical symptoms (average: AAV-Crry, 1.4 ± 0.3; AAV-EGFP, 1.5 ± 0.3), which was typically observed around day 11 post immunization (AAV-Crry, 11.2 ± 0.6; AAV-EGFP, 11.4 ± 0.4). Another cohort of mice was assessed at peak disease (average: AAV-Crry, 3 ± 0.45; AAV-EGFP, 2.66 ± 0.71), which was typically observed around day 18 post immunization.

Beginning with mice at the onset of EAE, we first determined the degree of EGFP colocalization with VGluT2$^+$-retinogeniculate terminals in the LGN and found ~45% of VGluT2$^+$-retinogeniculate terminals in the LGN colocalized with EGFP after injection of both AAVs (Figure 6D). We then immunostained for Crry protein and identified that Crry was highly enriched at presynaptic terminals within the LGN of AAV-Crry injected mice (Figures 6E and 6F), precisely where we identified enrichment of C3 (Figure 5). These data demonstrate successful CR2-mediated Crry targeting to retinogeniculate synapses bound by activated C3. In contrast, AAV-EGFP injected mice showed only diffuse Crry immunoreactivity with no concentration on or around presynaptic inputs in the LGN following EAE. Regardless of AAV treatment, mice showed comparable reactive gliosis, infiltration of peripheral immune cells, and C1q upregulation (Figures 6H and 7E–7J). These data suggest that retinogeniculate overexpression of Crry did not have global effects on inflammation. We next asked if Crry overexpression reduced deposition of C3 at the onset of EAE. While we found modest reductions in total C3 throughout the LGN in EAE AAV-Crry treated mice, there was a pronounced decrease in the colocalization of C3 with VGluT2$^+$-retinogeniculate terminals in AAV-Crry-treated EAE mice at the onset of disease compared to AAV-EGFP controls (Figure 6G). C3 colocalization with VGluT1$^+$-corticothalamic inputs was also reduced, but this decrease was less pronounced compared to VGluT2$^+$ terminals. These data demonstrate that AAV-Crry is highly localized to synapses within the retinogeniculate circuit, and it can block C3 localization at synapses during EAE.

Synapse-Localized Crry blocks Microglial Synapse Engulfment, Rescues Synapse Loss, and Restores Visual Function in Demyelinating Disease

Following validation that Crry is localized to retinogeniculate presynaptic terminals, where it inhibits C3 localization at synapses without more global effects on inflammation and reactive gliosis, we next assessed microglia-mediated synapse engulfment. Consistent with microglia-eliminating synapses via C3-mediated engulfment, there was a significant reduction in VGluT2$^+$ and VGluT1$^+$ terminals engulfed within microglial lysosomes of AAV-Crry-treated mice compared to AAV-EGFP controls (Figures 7K and 7L). We then measured synapse loss and identified a significant attenuation of VGluT2$^+$ and VGluT1$^+$ synapse loss at EAE onset (Figures 7M and 7N). We also assessed synapse engulfment and loss of presynaptic terminals in layer IV of the somatosensory cortex, a brain region without direct inputs from RGCs or the LGN, and identified that AAV-Crry did not protect these synapses (Figures S7A and S7B). These data suggest that the protective effects of AAV-mediated Crry expression are circuit specific. To assess long-term effects of AAV-Crry, we also assessed synapses at peak disease ± AAV-Crry in a separate cohort of EAE mice (Figure S6A). First, in control AAV-EGFP mice, synapse loss was still observed, and mild but significant demyelination, neuron loss, and axon degeneration became apparent in the retinogeniculate circuit at peak EAE (Figures S6B–S6D). However, in AAV-Crry mice, synapse loss was still protected at peak EAE, but demyelination, myelin engulfment by microglia, axon and neuron loss, gliosis, and peripheral immune cell infiltration were unaffected (Figures

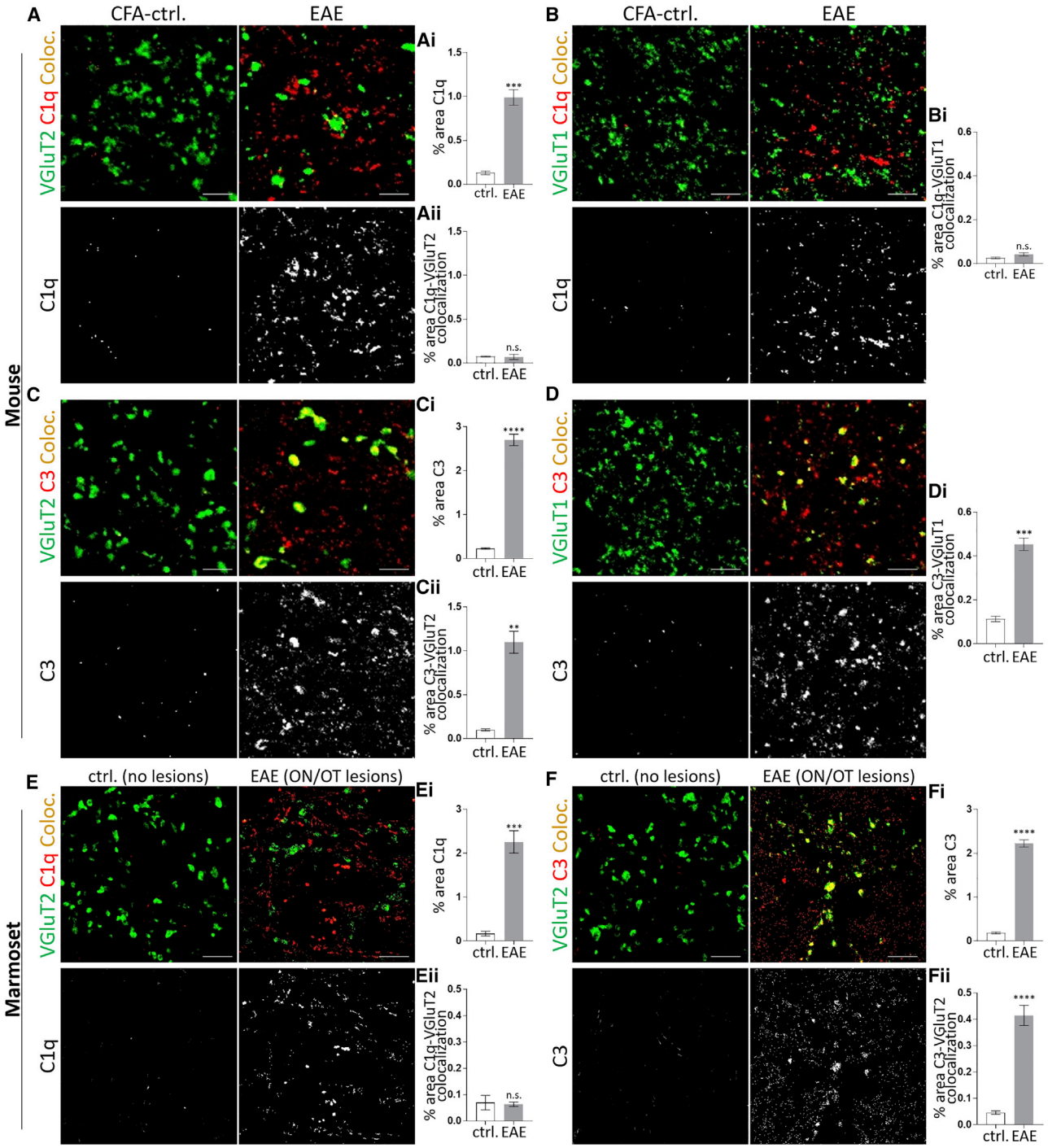

Figure 5. Complement Component C3, but Not C1q, Localizes to Synapses in Mouse and Marmoset EAE Models

(A–D) Representative confocal images of the same control and EAE mouse LGN shown in Figures 2, 3, and 4 immunostained against presynaptic (A and C) VGluT2 (green) or (B and D) VGluT1 (green) and complement component (A and B) C1q (red) or (C and D) C3 (red). Quantification of total (Ai) C1q and (Ci) C3 fluorescence area and colocalization of (Aii and Bi) C1q or (Cii and Di) C3 with presynaptic compartments in the LGN of CFA-ctrl. and EAE mice. n = 3 mice per condition from one experiment. Scale bars, 5 μm.

(E and F) Representative coronal sections of the LGN from the same control marmosets and animals that developed EAE with demyelinating lesions in the optic nerve and tract (ON/OT lesions) shown in Figure 1 stained against presynaptic VGluT2 (green) and (E) complement component C1q or (F) complement factor C3 (red). (Ei and Fi) Quantification of total (Ei) C1q and (Fi) C3 area, and colocalization (Eii and Fii) to VGluT2$^+$-presynaptic compartments in marmoset LGN. n = 4 marmosets per condition from two experiments. Scale bars, 5 μm.

Data represent mean ± SEM; significant differences with **p < 0.01, ***p < 0.001, ****p < 0.0001; t test. See also Figures S1, S2, and S3.

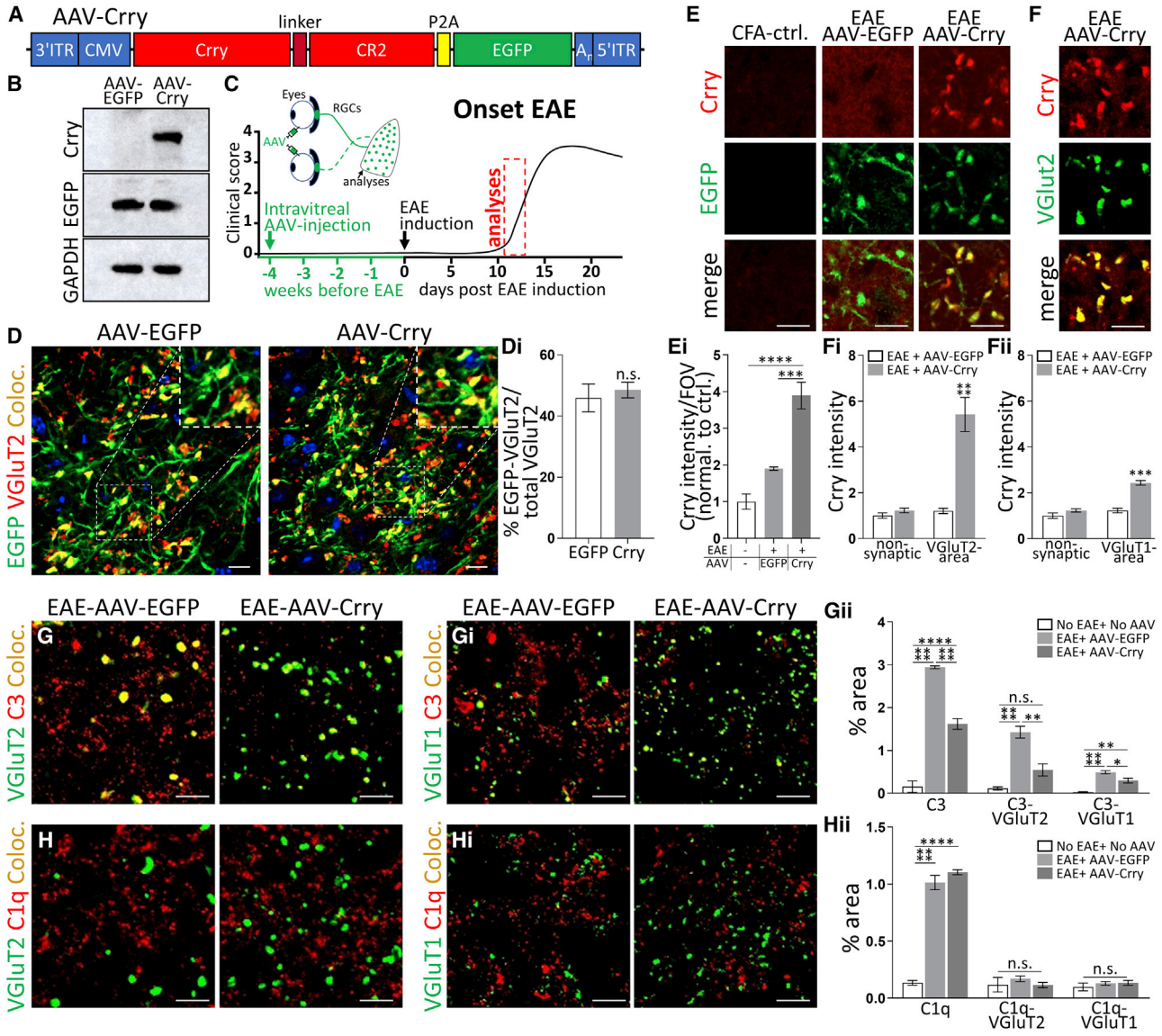

Figure 6. AAV9 Delivery of the C3 Inhibitor Crry Decreases Deposition of Synaptic C3

(A) Linear map of the AAV-Crry construct. ITR, inverted terminal repeat; CMV, human cytomegalovirus promotor; P2A, autocleavage site; A_n, polyadenylation signal.

(B) Representative immunoblots of Crry, EGFP, and GAPDH of homogenates from AAV-EGFP and AAV-Crry-EGFP (AAV-Crry)-transduced N2a cells.

(C) Timeline of *in vivo* AAV rescue experiments.

(D) Representative confocal images of the LGN of AAV-EGFP or AAV-Crry-EGFP (AAV-Crry) injected mice stained against EGFP (green) and presynaptic VGluT2 (red). DAPI, nuclei counterstain (blue). Scale bars, 10 μm. Inset shows magnified details. (Di) Colocalization (Coloc., yellow) analysis of EGFP with $VGluT2^+$-retinogeniculate terminals in AAV-EGFP and AAV-Crry treated mice.

(E) Representative confocal images of the LGN of CFA-ctrl. and EAE-induced mice that received intravitreal injections with AAV-EGFPs or AAV-Crry immunostained for Crry and EGFP. (Ei) Quantification of Crry fluorescence intensity (data normalized to CFA-ctrls.) in the LGN.

(F) Representative images of Crry and VGluT2 immunostaining in the LGN and (Fi and Fii) quantification of Crry intensities at presynaptic terminals (Fi, $VGluT2^+$ area; Fii, $VGluT1^+$ area) versus non-synaptic areas (Fi, $VGluT2^-$ area; Fii, $VGluT1^-$ area).

(G and H) Representative confocal images of the LGN of AAV-EGFP or AAV-Crry-treated EAE mice immunostained against presynaptic (G) VGluT2 or (Gi) VGluT1 (green) and complement factor C3 (red) and (H) presynaptic VGluT2 or (Hi) VGluT1 (green) and complement factor C1q (red). (Gii and Hii) Quantification of total and synapse-associated (Gii) C3 and (Hii) C1q in the LGN of AAV-EGFP- and AAV-Crry-treated EAE mice. Scale bars, 5 μm.

(D–H) n = 5 mice per condition from one experiment.

Data represent mean ± SEM; significant differences with *p < 0.05, **p < 0.01, ***p < 0.001, ****p < 0.0001; (D, F) t test; (E, G, H) ANOVA with Tukey's post hoc test. See also Figure S7.

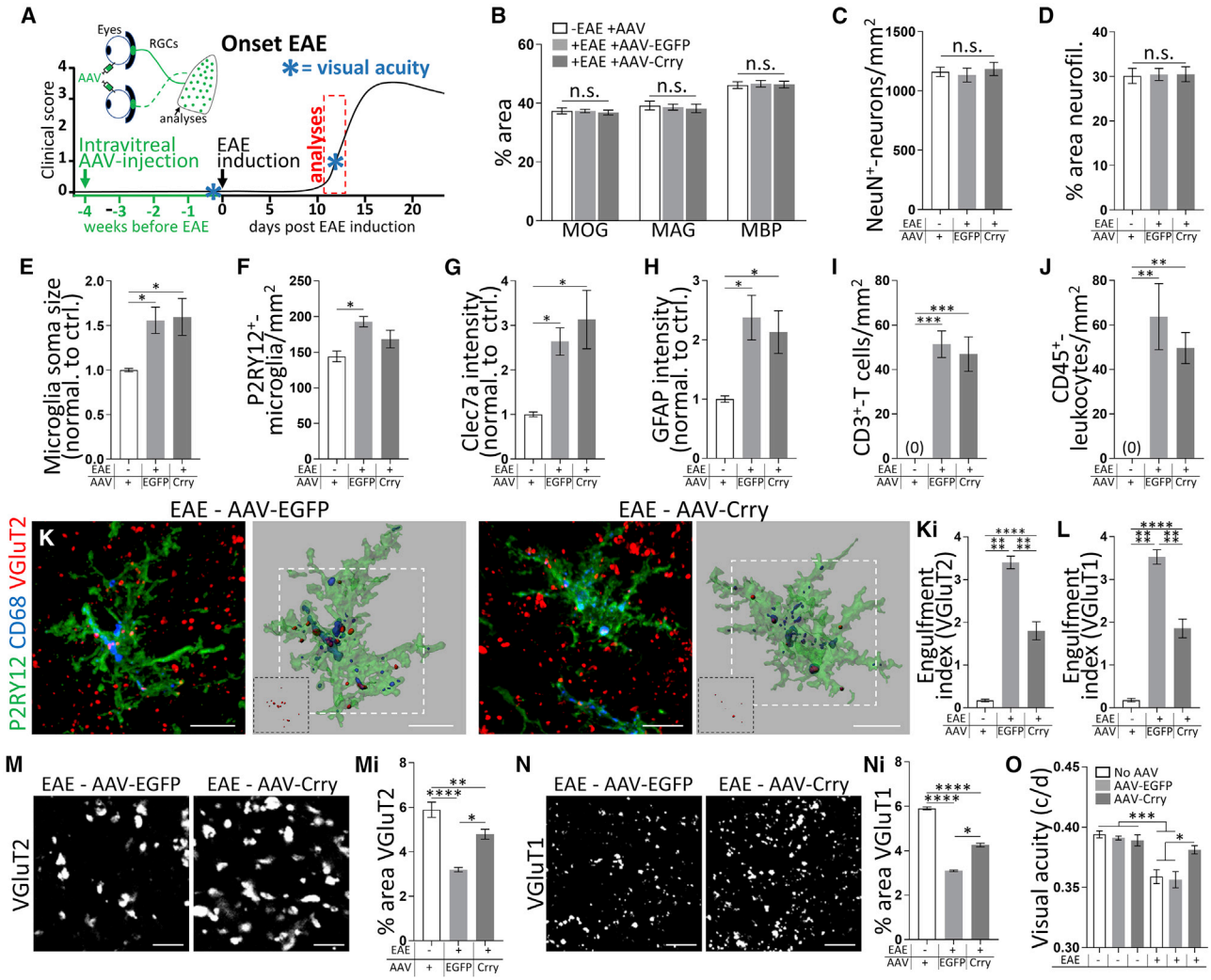

Figure 7. Synapse-Localized Crry Blocks Microglial Synapse Engulfment and Synapse Loss in the LGN and Restores Visual Function

(A) Timeline of *in vivo* AAV-rescue experiments.

(B–N) Analyses of adjacent LGN sections of onset EAE mice shown in Figure 6.

(B–D) Quantification of (B) MOG, MAG, and MBP; (C) NeuN$^+$ neuron; and (D) neurofilament$^+$-axon density following intraocular AAV injection in the EAE model.

(E–G) Quantification of (E) microglia soma size, (F) density of P2RY12$^+$ microglia, and (G) Clec7a intensity in AAV-treated mice in the EAE model.

(H–J) Further quantification of (H) GFAP$^+$-astrocytes, (I) CD3$^+$ T cells, and (J) CD45$^+$ leukocytes in AAV-treated mice in the EAE model.

(K and L) Representative images and 3D surface rendering of P2RY12$^+$-microglia (green) and engulfed VGluT2$^+$-retinogeniculate inputs (red) within CD68-labeled microglial lysosomes (blue). (Ki) Quantification of engulfed VGluT2$^+$-presynaptic inputs (red, inserts) and (L) VGluT1$^+$-presynaptic inputs within microglial lysosomes.

(M and N) Representative confocal images of the LGN of AAV-EGFP and AAV-Crry treated EAE mice immunostained against presynaptic (M) VGluT2 or (N) VGluT1 and (Mi and Ni) respective quantification.

(O) Visual acuity measured as spatial frequency threshold (cycles/degree) in the optomotor test before the induction of EAE (three left columns) and at the onset of clinical symptoms (three right columns) of the same control and AAV-EGFP or AAV-Crry transduced mice as shown in (B)–(N).

(B–J) n = 4, (K–N) n = 5, and (O) n = 5–8 mice per condition from one experiment. Scale bars, (K) 10 μm and (M and N) 5 μm. Data represent mean ± SEM; significant differences with *p < 0.05, **p < 0.01, ***p < 0.001, ****p < 0.0001; ANOVA with Tukey's post hoc test. See also Figure S7.

S6B–S6K and S7C). These data further support that synapse loss is a separable feature of the degenerative process in demyelinating disease.

Finally, to ask if protection of synapse loss in the retinogeniculate circuit has consequences for visual function, we assessed visual acuity (Prusky et al., 2004) in mice before induction of EAE and either at the onset of EAE or at peak disease by optomotor testing ± AAV transduction (Figures 7O and S6L). We first found that intravitreal injection of AAVs had no significant effect on visual acuity performance prior to EAE induction. We then observed a significant decline in visual acuity following EAE induction in all mice except the AAV-Crry treated cohorts. AAV-Crry treatment significantly blocked loss of visual acuity in mice at both the onset and peak of EAE. These data demonstrate that inhibition of C3 specifically at synapses protects circuit-specific structure and function. This represents a gene therapy

approach to inhibiting synapse loss, which may be broadly applicable to many neurodegenerative diseases where complement-dependent synapse loss has been implicated.

DISCUSSION

In postmortem human tissue, a preclinical nonhuman primate model of MS, and two rodent models of demyelinating disease, we identified microglial engulfment of presynaptic inputs and synapse loss in a MS-relevant visual circuit, the retinogeniculate circuit. We further provide evidence that this process can occur independent of axon degeneration and neuronal cell loss and, in the case of mouse EAE, in the absence of significant demyelination. Instead, synapse engulfment and loss in the visual thalamus occurred concomitant with local reactive gliosis and in the presence of synapse-enriched C3, but not synapse-associated C1q. Finally, overexpressing Crry, an inhibitor of C3, in the retinogeniculate circuit reduced synaptic C3, inhibited microglial synapse engulfment, and attenuated synapse loss specifically within the LGN with no significant effect on other pathologies. Together, these data support a model by which reactive microglia mediate synapse loss through the alternative complement cascade in demyelinating disease.

Our data showing that synapse engulfment and loss was in some cases independent of and/or prior to other MS-relevant pathologies is in line with previous work suggesting that gray matter degeneration in MS can at least partially occur independent of demyelination (Mandolesi et al., 2015). Also, there is evidence that even with the generation of new FDA-approved MS therapies, there is ''silent progression'' of the disease where a symptom-free patient at a 2-year follow up still develops significant disability by the 10th year (Cree et al., 2019). Local gliosis and microglia-mediated synapse elimination may be an underlying feature of this silent progression and an early event in the progressive course of neurodegeneration. Consistent with this idea, prior work implicates the thalamus as one of the earliest targets of degeneration in MS, and thalamic degeneration is an accurate predictor of subsequent MS-related disability (Eshaghi et al., 2018; Zivadinov et al., 2013). Work in mouse models of other neurodegenerative diseases have also shown similar early synapse loss when reactive microglia are also present (Hong et al., 2016; Lui et al., 2016; Paolicelli et al., 2017; Vasek et al., 2016; Wishart et al., 2006; Yoshiyama et al., 2007). In the current study, we further showed that these early synaptic changes in demyelinating disease occur in both males and females, but males trended toward more profound loss of synapses. This is consistent with the literature demonstrating that while MS is less frequent, males tend to have more aggressive disease with more disability compared to females (Bove et al., 2012; Confavreux et al., 2000; Gholipour et al., 2011). A further assessment of potential sex differences in severity of synapse loss and underlying mechanisms will be important going forward.

A question arising from our work relates to how inflammatory reactive microgliosis and synapse loss are initiated. One possibility is that there are more subtle changes in the myelin sheath and/or neural activity, which are responsible for triggering microglia-mediated synapse loss in demyelinating disease. Indeed, recent work has suggested that mice mutant for myelin genes with no detectable gross changes in the myelin sheath have low-grade inflammation and microgliosis (Janova et al., 2018). Another likely mechanism for initiation of microglia-mediated synapse loss is through blood-brain barrier breakdown and peripheral immune cell infiltration, which occurred in EAE and, to a lesser extent, in the DTA model. This potential mechanism is supported by a recent study showing that β-synuclein-specific T cells, which are also present in human MS cases, can induce local gliosis and cortical gray matter degeneration in mice (Lodygin et al., 2019). Similarly, T cells were shown to stimulate microglia-mediated synapse elimination in a mouse model of West Nile virus infection and neuron loss in Zika-infected mice (Garber et al., 2019). In addition to T cells, leakage of fibrinogen from the vasculature following blood-brain barrier breakdown has also been shown to regulate local microgliosis and axon degeneration in the spinal cord in mouse EAE and microglia-mediated dendritic spinal loss in the cortex in a mouse model of Alzheimer's disease (Davalos et al., 2012; Merlini et al., 2019; Szalai et al., 2007). The relative contribution of blood-brain barrier breakdown to initiation of complement-mediated synapse elimination by microglia in MS-relevant disease is a key question.

Another important consideration is the potential role of astrocytes and astrocyte-microglia crosstalk in the initiation of complement-mediated synapse engulfment and elimination. In development, similar to microglia, astrocytes engulf synaptic material and regulate synaptic architecture (Chung et al., 2013). Astrocytes also become phagocytic and engulf increased amounts of synaptic material following stroke-induced brain ischemia and other disease-relevant conditions (Morizawa et al., 2017; Bellesi et al., 2017; Chung et al., 2016). In contrast, we showed that synapse engulfment is mediated by microglia but not astrocytes. Our data are most consistent with recent work showing that reactive, neurotoxic astrocytes have decreased phagocytic capacity (Liddelow et al., 2017). However, this does not rule out the possibility that local astrogliosis can influence microglia-mediated synapse elimination in other ways. For example, astrocytes also promote microglial synaptic engulfment in the developing brain through interleukin (IL)-33 signaling (Vainchtein et al., 2018). In other models of neurodegeneration, microglia induce astrocytes to transition to a more reactive phenotype, including induction of astrocytic C3 (Liddelow et al., 2017). Understanding how these reactive astrocytes then, in turn, influence microglia-mediated synapse elimination will be an important direction to explore in the future.

A key finding in our study is the identification of a role for C3 and the alternative versus the classical complement cascade in retinogeniculate synapse elimination during inflammatory demyelinating disease. In contrast, the classical complement cascade molecules C1q and C3 localize to synapses and block microglial synapse engulfment and synapse elimination during developmental synaptic pruning (Schafer et al., 2012; Stevens et al., 2007; Bialas and Stevens, 2013) and in mouse models of Alzheimer's disease, frontotemporal dementia, and West Nile virus infection (Hong et al., 2016a; Vasek et al., 2016; Lui et al., 2016; Shi et al., 2017). Another recent study indicates that C1q and C3 increase in MS and may colocalize with synaptic proteins in postmortem MS brains (Michailidou et al., 2015). Our data indicated a similar increase in C1q but no C1q deposition at retinogeniculate synapses in multiple MS-relevant animal models. Instead, we observed localization of C3 to synapses. These

data suggest that synapse elimination occurs through the alternative, versus the C1q-dependent classical, complement cascade in demyelinating disease. This is consistent with earlier work in EAE suggesting that the alternative complement pathway predominates and that blocking this pathway globally prevents disease progression (Nataf et al., 2000). Similarly, clinical studies have shown increases in C3 in the plasma and CSF of MS patients, which correlates with disease severity and clinical disability (Ingram et al., 2012, 2014; Tatomir et al., 2017; Aeinehband et al., 2015). However, it is still important to consider the contribution of C1q in perhaps driving inflammatory-reactive gliosis. Related, the microglial receptor regulating engulfment of C3-opsonized synapses in our models remains to be identified. Mice deficient in CR3 display an ~50% block of microglial synaptic engulfment during developmental synaptic pruning and in a mouse model of Alzheimer's disease (Hong et al., 2016a; Schafer et al., 2012). CR 3a (C3aR), but not CR3, regulates microglial synapse engulfment in a West Nile-virus-induced model of synapse loss and cognitive impairment (Vasek et al., 2016). However, assessing synapse loss CR3 or C3aR-deficient mice is challenging, as both have attenuated EAE due to a dampened peripheral inflammatory response (Boos et al., 2004; Bullard et al., 2005). Therefore, the identification of microglial receptors involved in synapse engulfment in demyelinating disease requires new genetic tool development to more specifically manipulate these receptors in microglia versus other myeloid lineage cells.

Finally, using AAV-mediated *in vivo* gene delivery of Crry in mouse EAE, we showed that selective inhibition of activated C3 at presynaptic boutons protected structural synapses and visual function. This was achieved by overexpressing Crry fused to a domain of CR2 that only binds activated C3 in RGCs, resulting in enrichment of Crry protein in retinogeniculate presynaptic terminals following EAE. Supporting this as a possible therapeutic strategy, AAV-mediated delivery of Crry decreases C3 activation in models of macular degeneration and ischemic brain injury (Atkinson et al., 2005; 2006; Huang et al., 2008; Marshall et al., 2014; Alawieh et al., 2015). Also, systemic, peripheral administration of a Crry-CR2 encoding AAV attenuates EAE (Hu et al., 2012), which was attributed to the targeting of peripheral immune cells and restricting epitope spreading. This contrasts with our study where the AAV was delivered locally to the eye, resulting in specific reduction in C3 and protection of synapses in the retinogeniculate circuit with no significant attenuation of peripheral immune infiltration, increased C1q, or reactive gliosis. Further, at later time points during peak EAE, synapses were still protected, but the mild demyelination and axon degeneration in the retinogeniculate circuit in EAE were not. These data further support that synapse loss is an early pathology and is most consistent with Crry-AAV specifically inhibiting C3 at synapses in the LGN as compared to an indirect effect following decreases in, for example, reactive microgliosis. We also observed some, albeit milder, protection of $VGluT1^+$-corticothalamic synapses in the LGN, in addition to protection of $VGluT2^+$-retinogeniculate synapses. The Crry protein in our paradigm was not full length. Therefore, it is possible that Crry at retinogeniculate synapses was being released locally to protect $VGluT1^+$ synapses from elimination or that Crry modulated C3 production by astrocytes or microglial phagocytic capacity. In either case, these results demonstrate that Crry-mediated protection of synapses could be a viable therapeutic strategy to protect against synapse loss during neurodegeneration. While in some cases, synapse loss may be an endogenous protective mechanism to dampen activity and inhibit excitotoxicity, synapse loss may become dysregulated over the course of disease, leading to aberrant elimination of other "innocent bystander" synapses. This gives further support to developing a circuit-specific approach, such as AAV, to therapeutically target synapse loss in neurodegenerative disease.

STAR★METHODS

Detailed methods are provided in the online version of this paper and include the following:

- KEY RESOURCES TABLE
- LEAD CONTACT AND MATERIALS AVAILABILITY
- EXPERIMENTAL MODEL AND SUBJECT DETAILS
  - Mice and marmosets
  - Human samples
- METHOD DETAILS
  - Experimental autoimmune encephalomyelitis induction in marmosets
  - Experimental autoimmune encephalomyelitis induction in mice
  - Tamoxifen injections of DTA mice
  - Immunostaining of mouse tissue
  - Collection and immunostaining of human and marmoset tissue
  - Engulfment analysis
  - Synapse and complement density analyses
  - Density analysis of myelin, nodes, paranodes and axons
  - Cell density quantification
  - Fluorescence intensity analysis
  - Microglia soma size determination
  - RNA in situ hybridization
  - Electron microscopy and G-ratio determination
  - Generation of adeno-associated viral vector expressing Crry
  - Intravitreal injection of AAVs
  - Culture and treatment of neuro-2a cells
  - Western blot
  - Optomotor testing
- QUANTIFICATION AND STATISTICAL ANALYSIS
- DATA AND CODE AVAILABILITY

SUPPLEMENTAL INFORMATION

Supplemental Information can be found online at https://doi.org/10.1016/j.immuni.2019.12.004.

A video abstract is available at https://doi.org/10.1016/j.immuni.2019.12.004#mmc3.

ACKNOWLEDGMENTS

We thank Dr. Christopher C. Hemond (UMMS) for critical reading of the manuscript. We thank Dr. Paola Perrat (UMMS) for advice on the design and production of plasmids, Shannon Becker (UMMS) and Anoushka Lotun (UMMS) for assistance with tissue preparation, and Dr. Claudio Punzo and Georgia Gunner for advice and training on optomotor testing. We further thank

Prof. Dr. Matthew Rasband (Baylor College of Medicine) for sharing CASPR and βIV-spectrin specific antibodies and Prof. Oleg Butovsky for providing P2RY12 specific antibodies. This work was supported by Deutsche Forschungsgemeinschaft (DFG, Germany) grant WE 6170/1-1 (S.W.), NIMH—RO1MH113743 (D.P.S.), the Intramural Research Program of NINDS (D.S.R.), NINDS—R01NS099334 (B.P.), and the Dr. Miriam and Sheldon G. Adelson Medical Research Foundation (D.P.S., D.S.R., B.P., L.A.H.).

AUTHOR CONTRIBUTIONS

S.W. and D.P.S. designed the study and wrote the manuscript. S.W. performed and analyzed the experiments. J.J. assisted with mouse maintenance and conduction and analysis of experiments. S.J.C. and C.M.W. provided first murine EAE tissue and assisted in establishing the EAE mouse model. G.G. assisted with viral vector production. B.P. and R.B.K. maintained DTA mice and collected tissue for analyses. D.S.R. supervised collection and processing of human brain tissue by S.-K.H. and treatment and collection of marmoset tissue by N.J.L. N.P.B. and L.A.H. assisted with electron microscopy studies and measurements of G-ratios. All authors revised the manuscript for intellectually important content.

DECLARATION OF INTERESTS

The authors declare no conflict of interest.

Received: April 24, 2019
Revised: October 30, 2019
Accepted: December 11, 2019
Published: December 26, 2019

REFERENCES

Absinta, M., Sati, P., and Reich, D.S. (2016). Advanced MRI and staging of multiple sclerosis lesions. Nat. Rev. Neurol. *12*, 358–368.

Aeinehband, S., Lindblom, R.P., Al Nimer, F., Vijayaraghavan, S., Sandholm, K., Khademi, M., Olsson, T., Nilsson, B., Ekdahl, K.N., Darreh-Shori, T., and Piehl, F. (2015). Complement component C3 and butyrylcholinesterase activity are associated with neurodegeneration and clinical disability in multiple sclerosis. PLoS ONE *10*, e0122048.

Alawieh, A., and Tomlinson, S. (2016). Injury site-specific targeting of complement inhibitors for treating stroke. Immunol. Rev. *274*, 270–280.

Alawieh, A., Elvington, A., Zhu, H., Yu, J., Kindy, M.S., Atkinson, C., and Tomlinson, S. (2015). Modulation of post-stroke degenerative and regenerative processes and subacute protection by site-targeted inhibition of the alternative pathway of complement. J. Neuroinflammation *12*, 247.

Amato, M.P., Portaccio, E., Goretti, B., Zipoli, V., Hakiki, B., Giannini, M., Pastò, L., and Razzolini, L. (2010). Cognitive impairment in early stages of multiple sclerosis. Neurol. Sci. *31* (*Suppl 2*), S211–S214.

Araújo, S.E.S., Mendonça, H.R., Wheeler, N.A., Campello-Costa, P., Jacobs, K.M., Gomes, F.C.A., Fox, M.A., and Fuss, B. (2017). Inflammatory demyelination alters subcortical visual circuits. J. Neuroinflammation *14*, 162.

Atkinson, C., Song, H., Lu, B., Qiao, F., Burns, T.A., Holers, V.M., Tsokos, G.C., and Tomlinson, S. (2005). Targeted complement inhibition by C3d recognition ameliorates tissue injury without apparent increase in susceptibility to infection. J. Clin. Invest. *115*, 2444–2453.

Atkinson, C., Zhu, H., Qiao, F., Varela, J.C., Yu, J., Song, H., Kindy, M.S., and Tomlinson, S. (2006). Complement-dependent P-selectin expression and injury following ischemic stroke. J. Immunol. *177*, 7266–7274.

Bellesi, M., de Vivo, L., Chini, M., Gilli, F., Tononi, G., and Cirelli, C. (2017). Sleep Loss Promotes Astrocytic Phagocytosis and Microglial Activation in Mouse Cerebral Cortex. J. Neurosci. *37*, 5263–5273.

Bellizzi, M.J., Geathers, J.S., Allan, K.C., and Gelbard, H.A. (2016). Platelet-Activating Factor Receptors Mediate Excitatory Postsynaptic Hippocampal Injury in Experimental Autoimmune Encephalomyelitis. J. Neurosci. *36*, 1336–1346.

Bialas, A.R., and Stevens, B. (2013). TGF-β signaling regulates neuronal C1q expression and developmental synaptic refinement. Nat. Neurosci. *16*, 1773–1782.

Boos, L., Campbell, I.L., Ames, R., Wetsel, R.A., and Barnum, S.R. (2004). Deletion of the complement anaphylatoxin C3a receptor attenuates, whereas ectopic expression of C3a in the brain exacerbates, experimental autoimmune encephalomyelitis. J. Immunol. *173*, 4708–4714.

Bove, R.M., Healy, B., Augustine, A., Musallam, A., Gholipour, T., and Chitnis, T. (2012). Effect of gender on late-onset multiple sclerosis. Mult. Scler. *18*, 1472–1479.

Bullard, D.C., Hu, X., Schoeb, T.R., Axtell, R.C., Raman, C., and Barnum, S.R. (2005). Critical requirement of CD11b (Mac-1) on T cells and accessory cells for development of experimental autoimmune encephalomyelitis. J. Immunol. *175*, 6327–6333.

Butovsky, O., Jedrychowski, M.P., Moore, C.S., Cialic, R., Lanser, A.J., Gabriely, G., Koeglsperger, T., Dake, B., Wu, P.M., Doykan, C.E., et al. (2014). Identification of a unique TGF-β-dependent molecular and functional signature in microglia. Nat. Neurosci. *17*, 131–143.

Carroll, M.C. (1998). The role of complement and complement receptors in induction and regulation of immunity. Annu. Rev. Immunol. *16*, 545–568.

Chung, W.S., Clarke, L.E., Wang, G.X., Stafford, B.K., Sher, A., Chakraborty, C., Joung, J., Foo, L.C., Thompson, A., Chen, C., et al. (2013). Astrocytes mediate synapse elimination through MEGF10 and MERTK pathways. Nature *504*, 394–400.

Chung, W.S., Verghese, P.B., Chakraborty, C., Joung, J., Hyman, B.T., Ulrich, J.D., Holtzman, D.M., and Barres, B.A. (2016). Novel allele-dependent role for APOE in controlling the rate of synapse pruning by astrocytes. Proc. Natl. Acad. Sci. USA *113*, 10186–10191.

Ciotti, J.R., and Cross, A.H. (2018). Disease-Modifying Treatment in Progressive Multiple Sclerosis. Curr. Treat. Options Neurol. *20*, 12.

Coleman, P., Federoff, H., and Kurlan, R. (2004). A focus on the synapse for neuroprotection in Alzheimer disease and other dementias. Neurology *63*, 1155–1162.

Confavreux, C., Vukusic, S., Moreau, T., and Adeleine, P. (2000). Relapses and progression of disability in multiple sclerosis. N. Engl. J. Med. *343*, 1430–1438.

Cree, B.A.C., Hollenbach, J.A., Bove, R., Kirkish, G., Sacco, S., Caverzasi, E., Bischof, A., Gundel, T., Zhu, A.H., Papinutto, N., et al.; University of California, San Francisco MS-EPIC Team (2019). Silent progression in disease activity-free relapsing multiple sclerosis. Ann. Neurol. *85*, 653–666.

Crocker, S.J., Whitmire, J.K., Frausto, R.F., Chertboonmuang, P., Soloway, P.D., Whitton, J.L., and Campbell, I.L. (2006). Persistent macrophage/microglial activation and myelin disruption after experimental autoimmune encephalomyelitis in tissue inhibitor of metalloproteinase-1-deficient mice. Am. J. Pathol. *169*, 2104–2116.

Davalos, D., Ryu, J.K., Merlini, M., Baeten, K.M., Le Moan, N., Petersen, M.A., Deerinck, T.J., Smirnoff, D.S., Bedard, C., Hakozaki, H., et al. (2012). Fibrinogen-induced perivascular microglial clustering is required for the development of axonal damage in neuroinflammation. Nat. Commun. *3*, 1227.

Dutta, R., and Trapp, B.D. (2011). Mechanisms of neuronal dysfunction and degeneration in multiple sclerosis. Prog. Neurobiol. *93*, 1–12.

Dutta, R., Chang, A., Doud, M.K., Kidd, G.J., Ribaudo, M.V., Young, E.A., Fox, R.J., Staugaitis, S.M., and Trapp, B.D. (2011). Demyelination causes synaptic alterations in hippocampi from multiple sclerosis patients. Ann. Neurol. *69*, 445–454.

Eshaghi, A., Marinescu, R.V., Young, A.L., Firth, N.C., Prados, F., Jorge Cardoso, M., Tur, C., De Angelis, F., Cawley, N., Brownlee, W.J., et al. (2018). Progression of regional grey matter atrophy in multiple sclerosis. Brain *141*, 1665–1677.

Forner, S., Baglietto-Vargas, D., Martini, A.C., Trujillo-Estrada, L., and LaFerla, F.M. (2017). Synaptic Impairment in Alzheimer's Disease: A Dysregulated Symphony. Trends Neurosci. *40*, 347–357.

GBD 2016 Multiple Sclerosis Collaborators (2019). Global, regional, and national burden of multiple sclerosis 1990–2016: a systematic analysis for the Global Burden of Disease Study 2016. Lancet Neurol. *18*, 269–285.

Garber, C., Soung, A., Vollmer, L.L., Kanmogne, M., Last, A., Brown, J., and Klein, R.S. (2019). T cells promote microglia-mediated synaptic elimination and cognitive dysfunction during recovery from neuropathogenic flaviviruses. Nat. Neurosci. *22*, 1276–1288.

Gholipour, T., Healy, B., Baruch, N.F., Weiner, H.L., and Chitnis, T. (2011). Demographic and clinical characteristics of malignant multiple sclerosis. Neurology *76*, 1996–2001.

Gunner, G., Cheadle, L., Johnson, K.M., Ayata, P., Badimon, A., Mondo, E., Nagy, M.A., Liu, L., Bemiller, S.M., Kim, K.W., et al. (2019). Sensory lesioning induces microglial synapse elimination via ADAM10 and fractalkine signaling. Nat. Neurosci. *22*, 1075–1088.

Henstridge, C.M., Pickett, E., and Spires-Jones, T.L. (2016). Synaptic pathology: A shared mechanism in neurological disease. Ageing Res. Rev. *28*, 72–84.

Hong, Y.K., Park, S., Litvina, E.Y., Morales, J., Sanes, J.R., and Chen, C. (2014). Refinement of the retinogeniculate synapse by bouton clustering. Neuron *84*, 332–339.

Hong, S., Beja-Glasser, V.F., Nfonoyim, B.M., Frouin, A., Li, S., Ramakrishnan, S., Merry, K.M., Shi, Q., Rosenthal, A., Barres, B.A., et al. (2016a). Complement and microglia mediate early synapse loss in Alzheimer mouse models. Science *352*, 712–716.

Hong, S., Dissing-Olesen, L., and Stevens, B. (2016b). New insights on the role of microglia in synaptic pruning in health and disease. Curr. Opin. Neurobiol. *36*, 128–134.

Howell, O.W., Palser, A., Polito, A., Melrose, S., Zonta, B., Scheiermann, C., Vora, A.J., Brophy, P.J., and Reynolds, R. (2006). Disruption of neurofascin localization reveals early changes preceding demyelination and remyelination in multiple sclerosis. Brain *129*, 3173–3185.

Hu, X., Tomlinson, S., and Barnum, S.R. (2012). Targeted inhibition of complement using complement receptor 2-conjugated inhibitors attenuates EAE. Neurosci. Lett. *531*, 35–39.

Huang, Y., Qiao, F., Atkinson, C., Holers, V.M., and Tomlinson, S. (2008). A novel targeted inhibitor of the alternative pathway of complement and its therapeutic application in ischemia/reperfusion injury. J. Immunol. *181*, 8068–8076.

Ingram, G., Hakobyan, S., Robertson, N.P., and Morgan, B.P. (2009). Complement in multiple sclerosis: its role in disease and potential as a biomarker. Clin. Exp. Immunol. *155*, 128–139.

Ingram, G., Hakobyan, S., Hirst, C.L., Harris, C.L., Loveless, S., Mitchell, J.P., Pickersgill, T.P., Robertson, N.P., and Morgan, B.P. (2012). Systemic complement profiling in multiple sclerosis as a biomarker of disease state. Mult. Scler. *18*, 1401–1411.

Ingram, G., Loveless, S., Howell, O.W., Hakobyan, S., Dancey, B., Harris, C.L., Robertson, N.P., Neal, J.W., and Morgan, B.P. (2014). Complement activation in multiple sclerosis plaques: an immunohistochemical analysis. Acta Neuropathol. Commun. *2*, 53.

Janova, H., Arinrad, S., Balmuth, E., Mitjans, M., Hertel, J., Habes, M., Bittner, R.A., Pan, H., Goebbels, S., Begemann, M., et al. (2018). Microglia ablation alleviates myelin-associated catatonic signs in mice. J. Clin. Invest. *128*, 734–745.

Jordão, M.J.C., Sankowski, R., Brendecke, S.M., Sagar, Locatelli, G., Tai, Y.-H., Tay, T.L., Schramm, E., Armbruster, S., Hagemeyer, N., et al. (2019). Single-cell profiling identifies myeloid cell subsets with distinct fates during neuroinflammation. Science *363*.

Jürgens, T., Jafari, M., Kreutzfeldt, M., Bahn, E., Brück, W., Kerschensteiner, M., and Merkler, D. (2016). Reconstruction of single cortical projection neurons reveals primary spine loss in multiple sclerosis. Brain *139*, 39–46.

Keren-Shaul, H., Spinrad, A., Weiner, A., Matcovitch-Natan, O., Dvir-Szternfeld, R., Ulland, T.K., David, E., Baruch, K., Lara-Astaiso, D., Toth, B., et al. (2017). A Unique Microglia Type Associated with Restricting Development of Alzheimer's Disease. Cell *169*, 1276–1290.

Krasemann, S., Madore, C., Cialic, R., Baufeld, C., Calcagno, N., El Fatimy, R., Beckers, L., O'Loughlin, E., Xu, Y., Fanek, Z., et al. (2017). The TREM2-APOE Pathway Drives the Transcriptional Phenotype of Dysfunctional Microglia in Neurodegenerative Diseases. Immunity *47*, 566–581.

Lambris, J.D., and Tsokos, G.C. (1986). The biology and pathophysiology of complement receptors. Anticancer Res. *6* (3 Pt B), 515–523.

Lassmann, H. (2010). Axonal and neuronal pathology in multiple sclerosis: what have we learnt from animal models. Exp. Neurol. *225*, 2–8.

Lassmann, H. (2018). Multiple Sclerosis Pathology. Cold Spring Harb. Perspect. Med. *8*.

Lee, N.J., Ha, S.K., Sati, P., Absinta, M., Luciano, N.J., Lefeuvre, J.A., Schindler, M.K., Leibovitch, E.C., Ryu, J.K., Petersen, M.A., et al. (2018). Spatiotemporal distribution of fibrinogen in marmoset and human inflammatory demyelination. Brain *141*, 1637–1649.

Leibovitch, E.C., Caruso, B., Ha, S.K., Schindler, M.K., Lee, N.J., Luciano, N.J., Billioux, B.J., Guy, J.R., Yen, C., Sati, P., et al. (2018). Herpesvirus trigger accelerates neuroinflammation in a nonhuman primate model of multiple sclerosis. Proc. Natl. Acad. Sci. USA *115*, 11292–11297.

Liddelow, S.A., Guttenplan, K.A., Clarke, L.E., Bennett, F.C., Bohlen, C.J., Schirmer, L., Bennett, M.L., Münch, A.E., Chung, W.S., Peterson, T.C., et al. (2017). Neurotoxic reactive astrocytes are induced by activated microglia. Nature *541*, 481–487.

Lodygin, D., Hermann, M., Schweingruber, N., Flügel-Koch, C., Watanabe, T., Schlosser, C., Merlini, A., Körner, H., Chang, H.F., Fischer, H.J., et al. (2019). β-Synuclein-reactive T cells induce autoimmune CNS grey matter degeneration. Nature *566*, 503–508.

Lui, H., Zhang, J., Makinson, S.R., Cahill, M.K., Kelley, K.W., Huang, H.Y., Shang, Y., Oldham, M.C., Martens, L.H., Gao, F., et al. (2016). Progranulin Deficiency Promotes Circuit-Specific Synaptic Pruning by Microglia via Complement Activation. Cell *165*, 921–935.

Mahad, D.H., Trapp, B.D., and Lassmann, H. (2015). Pathological mechanisms in progressive multiple sclerosis. Lancet Neurol. *14*, 183–193.

Mandolesi, G., Gentile, A., Musella, A., Fresegna, D., De Vito, F., Bullitta, S., Sepman, H., Marfia, G.A., and Centonze, D. (2015). Synaptopathy connects inflammation and neurodegeneration in multiple sclerosis. Nat. Rev. Neurol. *11*, 711–724.

Marshall, K.M., He, S., Zhong, Z., Atkinson, C., and Tomlinson, S. (2014). Dissecting the complement pathway in hepatic injury and regeneration with a novel protective strategy. J. Exp. Med. *211*, 1793–1805.

Merlini, M., Rafalski, V.A., Rios Coronado, P.E., Gill, T.M., Ellisman, M., Muthukumar, G., Subramanian, K.S., Ryu, J.K., Syme, C.A., Davalos, D., et al. (2019). Fibrinogen Induces Microglia-Mediated Spine Elimination and Cognitive Impairment in an Alzheimer's Disease Model. Neuron *101*, 1099–1108.

Michailidou, I., Willems, J.G., Kooi, E.J., van Eden, C., Gold, S.M., Geurts, J.J., Baas, F., Huitinga, I., and Ramaglia, V. (2015). Complement C1q-C3-associated synaptic changes in multiple sclerosis hippocampus. Ann. Neurol. *77*, 1007–1026.

Michailidou, I., Naessens, D.M., Hametner, S., Guldenaar, W., Kooi, E.J., Geurts, J.J., Baas, F., Lassmann, H., and Ramaglia, V. (2017). Complement C3 on microglial clusters in multiple sclerosis occur in chronic but not acute disease: Implication for disease pathogenesis. Glia *65*, 264–277.

Milnerwood, A.J., and Raymond, L.A. (2010). Early synaptic pathophysiology in neurodegeneration: insights from Huntington's disease. Trends Neurosci. *33*, 513–523.

Molina, H. (2002). The murine complement regulator Crry: new insights into the immunobiology of complement regulation. Cell. Mol. Life Sci. *59*, 220–229.

Morgan, B.P., and Kavanagh, D. (2018). Introduction to complement in health and disease: novel aspects and insights. Semin. Immunopathol. *40*, 1–2.

Morizawa, Y.M., Hirayama, Y., Ohno, N., Shibata, S., Shigetomi, E., Sui, Y., Nabekura, J., Sato, K., Okajima, F., Takebayashi, H., et al. (2017). Reactive astrocytes function as phagocytes after brain ischemia via ABCA1-mediated pathway. Nat. Commun. *8*, 28.

Mucke, L., and Selkoe, D.J. (2012). Neurotoxicity of amyloid β-protein: synaptic and network dysfunction. Cold Spring Harb. Perspect. Med. *2*, a006338.

Nataf, S., Carroll, S.L., Wetsel, R.A., Szalai, A.J., and Barnum, S.R. (2000). Attenuation of experimental autoimmune demyelination in complement-deficient mice. J. Immunol. *165*, 5867–5873.

Paolicelli, R.C., Jawaid, A., Henstridge, C.M., Valeri, A., Merlini, M., Robinson, J.L., Lee, E.B., Rose, J., Appel, S., Lee, V.M., and et al. (2017). TDP-43 Depletion in Microglia Promotes Amyloid Clearance but Also Induces Synapse Loss. Neuron *95*, 297–308.

Prusky, G.T., Alam, N.M., Beekman, S., and Douglas, R.M. (2004). Rapid quantification of adult and developing mouse spatial vision using a virtual optomotor system. Invest. Ophthalmol. Vis. Sci. *45*, 4611–4616.

Qiao, F., Atkinson, C., Song, H., Pannu, R., Singh, I., and Tomlinson, S. (2006). Complement plays an important role in spinal cord injury and represents a therapeutic target for improving recovery following trauma. Am. J. Pathol. *169*, 1039–1047.

Reich, D.S., Lucchinetti, C.F., and Calabresi, P.A. (2018). Multiple Sclerosis. N. Engl. J. Med. *378*, 169–180.

Reis, E.S., Mastellos, D.C., Hajishengallis, G., and Lambris, J.D. (2019). New insights into the immune functions of complement. Nat. Rev. Immunol. *19*, 503–516.

Schafer, D.P., Lehrman, E.K., Kautzman, A.G., Koyama, R., Mardinly, A.R., Yamasaki, R., Ransohoff, R.M., Greenberg, M.E., Barres, B.A., and Stevens, B. (2012). Microglia sculpt postnatal neural circuits in an activity and complement-dependent manner. Neuron *74*, 691–705.

Schafer, D.P., Lehrman, E.K., Heller, C.T., and Stevens, B. (2014). An engulfment assay: a protocol to assess interactions between CNS phagocytes and neurons. J. Vis. Exp. (88).

Schafer, D.P., Heller, C.T., Gunner, G., Heller, M., Gordon, C., Hammond, T., Wolf, Y., Jung, S., and Stevens, B. (2016). Microglia contribute to circuit defects in Mecp2 null mice independent of microglia-specific loss of Mecp2 expression. eLife *5*.

Selkoe, D.J. (2002). Alzheimer's disease is a synaptic failure. Science *298*, 789–791.

Selkoe, D.J., Triller, A., and Christen, Y. (2008). Synaptic plasticity and the mechanism of Alzheimer's disease (Berlin: Springer).

Shi, Y., Yamada, K., Liddelow, S.A., Smith, S.T., Zhao, L., Luo, W., Tsai, R.M., Spina, S., Grinberg, L.T., Rojas, J.C., et al.; Alzheimer's Disease Neuroimaging Initiative (2017). ApoE4 markedly exacerbates tau-mediated neurodegeneration in a mouse model of tauopathy. Nature *549*, 523–527.

Stevens, B., Allen, N.J., Vazquez, L.E., Howell, G.R., Christopherson, K.S., Nouri, N., Micheva, K.D., Mehalow, A.K., Huberman, A.D., Stafford, B., et al. (2007). The classical complement cascade mediates CNS synapse elimination. Cell *131*, 1164–1178.

Szalai, A.J., Hu, X., Adams, J.E., and Barnum, S.R. (2007). Complement in experimental autoimmune encephalomyelitis revisited: C3 is required for development of maximal disease. Mol. Immunol. *44*, 3132–3136.

Tatomir, A., Talpos-Caia, A., Anselmo, F., Kruszewski, A.M., Boodhoo, D., Rus, V., and Rus, H. (2017). The complement system as a biomarker of disease activity and response to treatment in multiple sclerosis. Immunol. Res. *65*, 1103–1109.

Toosy, A.T., Mason, D.F., and Miller, D.H. (2014). Optic neuritis. Lancet Neurol. *13*, 83–99.

Traka, M., Arasi, K., Avila, R.L., Podojil, J.R., Christakos, A., Miller, S.D., Soliven, B., and Popko, B. (2010). A genetic mouse model of adult-onset, pervasive central nervous system demyelination with robust remyelination. Brain *133*, 3017–3029.

Traka, M., Podojil, J.R., McCarthy, D.P., Miller, S.D., and Popko, B. (2016). Oligodendrocyte death results in immune-mediated CNS demyelination. Nat. Neurosci. *19*, 65–74.

Turnberg, D., and Botto, M. (2003). The regulation of the complement system: insights from genetically-engineered mice. Mol. Immunol. *40*, 145–153.

Tyebji, S., and Hannan, A.J. (2017). Synaptopathic mechanisms of neurodegeneration and dementia: Insights from Huntington's disease. Prog. Neurobiol. *153*, 18–45.

Vainchtein, I.D., Chin, G., Cho, F.S., Kelley, K.W., Miller, J.G., Chien, E.C., Liddelow, S.A., Nguyen, P.T., Nakao-Inoue, H., Dorman, L.C., et al. (2018). Astrocyte-derived interleukin-33 promotes microglial synapse engulfment and neural circuit development. Science *359*, 1269–1273.

Vasek, M.J., Garber, C., Dorsey, D., Durrant, D.M., Bollman, B., Soung, A., Yu, J., Perez-Torres, C., Frouin, A., Wilton, D.K., et al. (2016). A complement-microglial axis drives synapse loss during virus-induced memory impairment. Nature *534*, 538–543.

Voet, S., Prinz, M., and van Loo, G. (2019). Microglia in Central Nervous System Inflammation and Multiple Sclerosis Pathology. Trends Mol. Med. *25*, 112–123.

Watkins, L.M., Neal, J.W., Loveless, S., Michailidou, I., Ramaglia, V., Rees, M.I., Reynolds, R., Robertson, N.P., Morgan, B.P., and Howell, O.W. (2016). Complement is activated in progressive multiple sclerosis cortical grey matter lesions. J. Neuroinflammation *13*, 161.

Weideman, A.M., Tapia-Maltos, M.A., Johnson, K., Greenwood, M., and Bielekova, B. (2017). Meta-analysis of the Age-Dependent Efficacy of Multiple Sclerosis Treatments. Front. Neurol. *8*, 577.

Weinhard, L., di Bartolomei, G., Bolasco, G., Machado, P., Schieber, N.L., Neniskyte, U., Exiga, M., Vadisiute, A., Raggioli, A., Schertel, A., et al. (2018). Microglia remodel synapses by presynaptic trogocytosis and spine head filopodia induction. Nat. Commun. *9*, 1228.

Wishart, T.M., Parson, S.H., and Gillingwater, T.H. (2006). Synaptic vulnerability in neurodegenerative disease. J. Neuropathol. Exp. Neurol. *65*, 733–739.

Wolswijk, G., and Balesar, R. (2003). Changes in the expression and localization of the paranodal protein Caspr on axons in chronic multiple sclerosis. Brain *126*, 1638–1649.

Yoshiyama, Y., Higuchi, M., Zhang, B., Huang, S.M., Iwata, N., Saido, T.C., Maeda, J., Suhara, T., Trojanowski, J.Q., and Lee, V.M. (2007). Synapse loss and microglial activation precede tangles in a P301S tauopathy mouse model. Neuron *53*, 337–351.

Zivadinov, R., Havrdová, E., Bergsland, N., Tyblova, M., Hagemeier, J., Seidl, Z., Dwyer, M.G., Vaneckova, M., Krasensky, J., Carl, E., et al. (2013). Thalamic atrophy is associated with development of clinically definite multiple sclerosis. Radiology *268*, 831–841.

STAR★METHODS

KEY RESOURCES TABLE

REAGENT or RESOURCE	SOURCE	IDENTIFIER
Antibodies		
Mouse mAb α-ALDH1L1 (clone N103/39)	Millipore	Cat. #MABN495; RRID: AB_2687399
Mouse mAb α-APP (clone 22C11)	Millipore	Cat. #MAB348; RRID: AB_94882
Rabbit mAb α-C1q (clone 4.8)	Abcam	Cat. #ab182451; RRID: AB_2732849
Rabbit pAb α-C1q (human/marmoset tissue)	Biologicals	Cat. #NBP1-87492; RRID: AB_11002443
Rat mAb α-C3 (clone 11H-9)	Abcam	Cat. #ab11862; RRID: AB_2066623
Mouse mAb α-C3d (clone 7C10) (human / marmoset tissue)	Abcam	Cat. #ab17453; RRID: AB_443879
Rabbit pAb α-CASPR	Matthew N. Rasband, Baylor College of Medicine, Houston. TX, USA	N/A
Rabbit mAb α-CD3 (clone SP7)	Abcam	Cat. #ab16669; RRID: AB_443425
Mouse mAb α-CD8 (clone 8/144B)	Thermo Fisher Scientific	Cat. #MA5-13473; RRID: AB_11000353
Rat mAb α-CD45 (clone IBL-3/16)	BioRad	Cat. #MCA1388; RRID: AB_321729
Mouse mAb α-CD68 (clone KP1)	Abcam	Cat. #ab955; RRID: AB_307338
Rat mAb α-CD68 (clone FA-11)	AbD Serotec	Cat. #MCA1957; RRID: AB_322219
Rat mAb α-Clec7a	InvivoGen	Cat. #mabg-mdect; RRID: AB_2753143
Rabbit pAb α-Clec12a	LSBio	Cat. #LS-C377776; RRID: AB_2819090
Rabbit pAb α-cleaved caspase-3	Cell Signaling Technologies	Cat. #9661; RRID: AB_2341188
Mouse mAb α-Crry (clone TLD-1C11)	Santa Cruz	Cat. #sc-53530; RRID: AB_2085157
Chicken pAb α-EGFP	Abcam	Cat. #ab13970; RRID: AB_300798
Rabbit pAb α-EGFP	Millipore	Cat. #ab3080P; RRID: AB_2630379
Mouse mAb α-FoxP3 (clone 206D)	BioLegend	Cat. #320102; RRID: AB_430881
Goat pAb α-GAPDH	Abcam	Cat. #ab9483; RRID: AB_307273
Mouse mAb α-GFAP (clone G-A-5)	Sigma	Cat. #G3893; RRID: AB_477010
Rabbit pAb α-Homer1	Synaptic Systems	Cat. #160003; RRID: AB_887730
Rabbit pAb α-Iba1	Wako Chemicals	Cat. #019-19741; RRID: AB_839504
Goat pAb α-Iba1 (human/marmoset tissue)	Abcam	Cat. #ab5076; RRID: AB_2224402
Rat mAb α-LAMP2 (clone GL2A7)	Abcam	Cat. #ab13524; RRID: AB_2134736
Rat mAb α-Ly6C (clone HK1.4)	BioLegend	Cat. #128016; RRID: AB_1732076
Mouse mAb α-MAG (clone 513)	Millipore	Cat. #MAB1567; RRID: AB_2137847
Chicken pAb α-MAP2 (marmoset tissue)	EnCor Biotechnology	Cat. #CPCA-MAP2; RRID: AB_2138173
Rat mAb α-MBP (clone 12)	Millipore	Cat. #MAB386; RRID: AB_94975
Mouse mAb α-MOG (clone 8-18C5)	Millipore	Cat. #MAB5680; RRID: AB_1587278
Rabbit pAb α-Neurofilament 200	Sigma	Cat. #N4142; RRID: AB_477272
Chicken pAb α-NeuN	Millipore	Cat. #ABN91; RRID: AB_11205760
Rabbit pAb α-P2RY12	AnaSpec	Cat. #AS-55043A; RRID: AB_2298886
Rat mAb α-P2RY12 (clone S16007D)	BioLegend	Cat. #848002; RRID: AB_2650634
Mouse mAb α-PSD-95 (clone 6G6-1C9)	Millipore	Cat. #MAB1596; RRID: AB_2092365
Guinea pig pAb α-RBPMS	PhosphoSolutions	Cat. #1832-RBPMS; RRID: AB_2492226
Rabbit pAb α-βIV-spectrin	Matthew N. Rasband, Baylor College of Medicine, Houston. TX, USA	N/A
Guinea pig pAb α-VGluT1	Millipore	Cat. #ab5905, RRID: AB_2301751
Rabbit pAb α-VGluT1 (human/marmoset tissue)	Millipore	Cat. #ABN1627; RRID: AB_2814811

(*Continued on next page*)

Continued

REAGENT or RESOURCE	SOURCE	IDENTIFIER
Guinea pig pAb α-VGluT2	Millipore	Cat. #ab2251; RRID: AB_1587626
Bacterial and Virus Strains		
AAV-Crry-EGFP (AAV9)	This paper	N/A
AAV-ctrl.-EGFP (AAV9)	This paper	N/A
Stbl3 chemically competent *E. coli*	Thermo Fisher Scientific	Cat. #C737303
Biological Samples		
Human brain tissue	Daniel S. Reich, Translational Neuroradiology Section, NINDS, NIH, Bethesda, MD, USA	N/A
Human white matter homogenate	Daniel S. Reich, NINDS, NIH, Bethesda, MD, USA	N/A
Chemicals, Peptides, and Recombinant Proteins		
4-hydroxytamoxifen	Sigma	Cat. #T176
All trans-retinoic acid	Sigma	Cat. #R2625
Complete Freund's adjuvant (mice)	Sigma	Cat. #F5881
Complete Freund's adjuvant (marmoset)	Absinta et al., 2016; Lee et al., 2018; Leibovitch et al., 2018	N/A
MOG_{35-55} peptide	AnaSpec Inc	Cat. #AS-60130
Mycobacterium tuberculosis H37Ra	Difco Laboratories	Cat. #231141
Glutaraldehyde	Ted Pella	Cat. #18426
Paraformaldehyde	Electron Microscopy Sciences	Cat. # 15710
Pertussis toxin	List Biologicals	Cat. #180
Critical Commercial Assays		
NEBuilder HiFi DNA assembly cloning kit	New England Biolabs	Cat. #E2621L
QIAfilter Plasmid Mega Kit	QIAGEN, #12281	Cat. #12281
RNAscope Multiplex Fluorescent Detection Kit	ACDBio	Cat. #320850
Experimental Models: Cell Lines		
Neuro-2a cells (N2a cells)	ATCC	Cat. #CCL-131
Experimental Models: Organisms/Strains		
Mouse: C57BL/6J	The Jackson Laboratory	Cat. #000664
Mouse: *Plp1-CreER^T;ROSA26-EGFP-DTA* and *ROSA26-EGFP-DTA* littermates	Brian Popko, University of Chicago. Chicago, IL, USA. (Traka et al., 2010, 2016)	N/A
Marmoset: *Callithrix jacchus*	Daniel S. Reich, NINDS, NIH, Bethesda, MD, USA. (Absinta et al., 2016; Lee et al., 2018; Leibovitch et al., 2018)	N/A
Oligonucleotides		
RNA *in situ* probes against *Il-6*	ACDBio	Cat. #315891
RNA *in situ* probes against *Il-1β*	ACDBio	Cat. #316891
Recombinant DNA		
pAAV-CB6-PI	Gene Therapy Center, UMass Medical School, Worcester, MA, USA	N/A
gBlock 1, encoding the sequence for the mature murine Crry protein (residues 1-319, GenBank accession number NM013499)	This paper (generated through IDT)	N/A

(*Continued on next page*)

Continued

REAGENT or RESOURCE	SOURCE	IDENTIFIER
gBlock 2, encoding the sequence for a (G4S)2 linker directly fused to a sequence encoding 4 N-terminal short consensus repeats of a CR2-sequence (residues 1-257, GenBank accession number M35684) followed by the sequence of a porcine teschovirus-1 2A (P2A) autocleavage site and the sequence for EGFP (both sequences from https://nebuilder.neb.com)	This paper (generated through IDT)	N/A
Software and Algorithms		
Graph Pad Prism v8.3.0	GraphPad Software	https://www.graphpad.com/
ImageJ v1.52k	NIH	https://imagej.nih.gov/ij/
Imaris v8.1.2	Bitplane	https://imaris.oxinst.com/
NEBuilder Assembly Tool v2.0.8	New England Biolabs	https://nebuilder.neb.com
Zen blue imaging software v2.3	Zeiss	https://www.zeiss.com/
Zen black acquisition software v8.1.11.484	Zeiss	https://www.zeiss.com/

LEAD CONTACT AND MATERIALS AVAILABILITY

Further information and requests for resources and reagents should be directed to and will be fulfilled by the Lead Contact, Dorothy Schafer (dorothy.schafer@umassmed.edu). AAV-Crry was produced in our laboratory and is available upon request to the Lead Contact with a completed Materials Transfer Agreement.

EXPERIMENTAL MODEL AND SUBJECT DETAILS

Mice and marmosets

Male and female wildtype C57BL/6J mice (stock #000664) were obtained from Jackson Laboratories (Bar Harbor, ME). Male *Plp1-CreER^T;ROSA26-EGFP-DTA* (DTA) and *ROSA26-EGFP-DTA* (DTA-ctrl.) littermates were generated by breeding hemizygous *Plp1-CreER^T* mice *with ROSA26-EGFP-DTA* homozygous mice (Traka et al., 2010, 2016). *5-8-week-old mice and their respective* littermate controls were used for all mouse experiments. 12 adult common marmosets (*Callithrix jacchus*), eight females and four males, were selected from the NINDS colony. All animal experiments were performed in accordance with Animal Care and Use Committees (IACUC) and under NIH guidelines for proper animal welfare.

Human samples

Collection of human postmortem brain tissue was performed after obtaining informed consent for collection. Tissue collection followed protocols approved by NIH Institutional Review Board. Samples analyzed in the current study were collected from 5 male and 5 female human subjects with ages ranging from 59-84 and 58-78 years, respectively. From these subjects, control samples were collected from 2 males and 3 females without diagnosed neurological disease, and MS samples were collected from 3 male and 2 female patients with progressive MS. See Table S1 for further details.

METHOD DETAILS

Experimental autoimmune encephalomyelitis induction in marmosets

EAE was induced in marmosets by injecting human white matter homogenate emulsified in complete Freund's adjuvant (Difco Laboratories, BD, Franklin Lakes, NJ, USA) (Absinta et al., 2016; Lee et al., 2018). For EAE induction, intradermal injections were divided over four areas around the inguinal and axillary lymph nodes. To conserve animals, marmoset tissue used in this study was drawn from prior studies, some of which were designed to examine the effects of intranasal inoculation of human herpesvirus (HHV)-6 on EAE development. Therefore, a subset of marmosets (EAE and non-EAE) used in our study also received either HHV6 serotype A derived from SUP-T1 cells, HHV6 serotype B derived from HSB-2 cells, or were inoculated with uninfected control SUP-T1 cells. Importantly, although the onset of EAE was accelerated with HHV6 treatment, no pathological changes in or outside of lesions other than accumulation of viral material were observed in the HHV6 studies (Leibovitch et al., 2018). Marmoset demyelinating lesions were monitored *in vivo* and *ex vivo* (i.e., postmortem dissected brain) by MRI. The animals were subsequently divided into 2 groups. The experimental group included EAE marmosets with clear demyelinating lesions in the optic nerve and tract. The control group were either EAE or non-EAE marmosets with no evidence of demyelinating lesions in the optic nerve or tract.

Experimental autoimmune encephalomyelitis induction in mice

As described previously (Crocker et al., 2006), experimental autoimmune encephalomyelitis (EAE) was induced in 8-week-old male and female mice, by subcutaneous (s.c.) administration of 200 μg of MOG_{35-55} peptide (AnaSpec, AS-60130-10, Fremont, CA, USA) emulsified in complete Freund's Adjuvant (CFA, Sigma, F5881, Saint Louise, MO, USA) containing 0.2 mg of *Mycobacterium tuberculosis* H37Ra (Difco Laboratories, #231141 Detroit, MI, USA) into the flanks of both hind-limbs. Control animals received s.c. injections lacking MOG_{35-55} peptide. At the time of immunization and 48 h later, mice further received intraperitoneal (i.p.) injections with 500 ng of pertussis toxin (List Biologicals, #180, Deisenhofen, Germany). Weights and clinical scores were recorded daily (score 0.5: distal tail limpness; score 1: complete limp tail; score 1.5: limp tail and hindlimb weakness; score 2: mild hindlimb paresis; score 2.5: unilateral hindlimb paralysis; score 3: bilateral hindlimb paralysis, score 4: moribund). For the EAE experiments presented in this study, mice were either analyzed at the onset of EAE, when animals displayed moderate clinical scores (typically observed between day 10-12 post immunization) or at peak disease when mice displayed severe clinical scores (typically observed ~18 days post induction). None of the CFA-treated control mice developed clinical symptoms.

Tamoxifen injections of DTA mice

Male *Plp1-CreER^T;ROSA26-EGFP-DTA* mice 5-7-week-old were injected intraperitoneally with 0.8 mg of 4-hydroxytamoxifen (Sigma) per day for four consecutive days, as previously described, to induce demyelination driven by genetic ablation of mature oligodendrocytes (Traka et al., 2010, 2016). Tamoxifen-injected ROSA26-EGFP-DTA littermates were used as control mice.

Immunostaining of mouse tissue

At the indicated time points, mice were deeply anesthetized and transcardially perfused with 0.1M phosphate buffer (PB) followed by 4% paraformaldehyde (PFA)/0.1M PB. Brains, retinas, and optic nerves were dissected, and brains and retinas were post-fixed at 4°C in PFA for 4 h and 30 min, respectively. Brains and optic nerves were then equilibrated in 30% sucrose/0.1M PB, and then embedded in a 1:1 mixture of 30% sucrose/0.1M PB and O.C.T. compound (ThermoFisher Scientific Waltham, MA, USA). Tissue was cryo-sectioned into 10 μm coronal brain sections and longitudinal optic nerve sections. Sections and whole retinas were blocked and permeabilized at room temperature for 1 h in 10% normal goat serum/0.1M PB containing 0.3% Triton X-100 (all Sigma) followed by overnight incubation with primary antibodies at room temperature. The following primary monoclonal (mAb) and polyclonal (pAb) antibodies have been used: mouse mAb α-ALDH1L1 (clone N103/39, Millipore, MABN495, 1:1000), mouse mAb α-APP (clone 22C11, Millipore, MAB348, 1:200), rabbit mAb α-C1q (clone 4.8, Abcam, ab182451, 1:100), rat mAb α-C3 (clone 11H-9, Abcam, ab11862, 1:500), rabbit pAb α-CASPR (provided by Matthew N. Rasband, 1:100), rabbit mAb α-CD3 (clone SP7, Abcam, ab16669, 1:100), mouse mAb α-CD8 (clone 8/114B, Thermo Fisher Scientific, MA5-13473, 1:20), rat mAb α-CD45 (clone IBL-3/16, BioRad, MCA1388, 1:100), mouse mAb α-CD68 (clone KP1, Abcam, ab955, 1:200), rat mAb α-CD68 (clone FA-11, AbD Serotec, MCA1957, 1:1000), rat mAb α-Clec7a (InvivoGen, mabg-mdect, 1:200), rabbit pAb α-Clec12a (LSBio, LS-C377776, 1:500), rabbit pAb α-cleaved caspase-3 (Cell Signaling Technologies, #9661, 1:200), mouse mAb α-Crry (clone TLD-1C11, Santa Cruz, sc-53530, 1:100), chicken pAb α-EGFP (Abcam, ab13970, 1:500), mouse mAb α-FoxP3 (clone 206D, BioLegend, 320102, 1:50), mouse mAb α-GFAP (clone G-A-5, Sigma, G3893, 1:500), rabbit pAb α-Homer1 (Synaptic Systems, #160003, 1:1000), rabbit pAb α-Iba1 (Wako Chemicals, #019-19741, 1:500), rat mAb α-LAMP2 (clone GL2A7, Abcam, ab13524, 1:200), rat mAb α-Ly6C (clone HK1.4, BioLegend, 128016, 1:300), mouse mAb α-MAG (clone 513, Millipore, MAB1567, 1:100), rat mAb α-MBP (clone 12, Millipore, MAB386, 1:500), mouse mAb α-MOG (clone 8-18C5, Millipore, MAB5680, 1:200), rabbit pAb α-Neurofilament 200 (Sigma, N4142, 1:1000), chicken pAb α-NeuN (Millipore, ABN91, 1:1000), rabbit pAb α-P2RY12 (AnaSpec, AS-55043A, 1:2000), rat mAb α-P2RY12 (clone S16007D, BioLegend, 848002, 1:100), mouse mAb α-PSD-95 (clone 6G6-1C9, Millipore, MAB1596, 1:100), guinea pig pAb α-RBPMS (PhosphoSolutions, 1832-RBPMS, 1:500), rabbit pAb α-βIV-spectrin (provided by Matthew N. Rasband, 1:100), guinea pig pAb α-VGluT1 (Millipore, ab5905, 1:2000), and guinea pig pAb α-VGluT2 (Millipore, ab2251, 1:2000). The following day, sections were incubated with appropriate Alexa-fluorophore-conjugated secondary antibodies (ThermoFisher Scientific) and mounted with vectashield containing DAPI (Vector laboratories, Burlingame, CA, USA).

Collection and immunostaining of human and marmoset tissue

Human postmortem brain tissue was dissected and formalin-fixed at autopsy and marmoset brains were collected within 1 h of death and fixed in 4% paraformaldehyde. Once individual slabs containing the lateral geniculate nucleus (LGN) of human and marmoset brains were identified, tissue was embedded in paraffin and sliced into 10 μm thick slides. For immunohistological stains on marmoset and human tissue, slices were deparaffinized and rehydrated, and antigen-binding sites were retrieved by heating for 1 h in 10 mM citrate buffer, pH 6.0, with 0.05% Tween-20 in a steam oven before staining. All subsequent steps followed the above described protocol for staining of mouse tissue. If goat-derived primary antibodies were used, blocking was performed with 10% donkey serum (Sigma). Different from staining of mouse tissue (see below), rabbit pAb α-C1q (Biologicals, NBP1-87492, 1:200) and mouse mAb α-C3d (clone 7C10, Abcam, ab17453, 1:50) were used to detect complement components, chicken pAb α-MAP2 (EnCor Biotechnology, CPCA-MAP2, 1:1000) was used to stain neurons, rabbit pAb α-VGluT1 (Millipore, abN1627) was used to label presynaptic corticothalamic inputs and goat pAb α-Iba1 (Abcam, ab5076, 1:200) was used to visualize microglia/macrophages on human and marmoset tissue.

Engulfment analysis

Engulfment analysis was performed according to previously described protocols (Schafer et al., 2012, 2014). Briefly, two sections from each sample containing the LGN in marmoset and human and the dorsal LGN in mouse were immunostained and imaged on a Zeiss Observer Spinning Disk Confocal microscope equipped with diode lasers (405 nm, 488 nm, 594 nm, 647 nm) and Zen Blue acquisition software (Zeiss; Oberkochen, Germany). For each hemisphere, 2-3 randomly chosen 63x fields of view within the dorsal lateral geniculate nucleus were acquired with 50-70 z stack steps at 0.22 μm optimal spacing using identical settings. Images were then processed in ImageJ (NIH) and individual images of 15-20 single cells per animal were processed in Imaris (Bitplane; Zurich, Switzerland) as previously described (Schafer et al., 2012, 2014). Engulfment analysis was restricted to synaptic material within CD68-positive microglial lysosomes or LAMP2-positive astrocytic lysosomes. Unbiased quantification of all images was performed blind to genotype or treatment of animals.

Synapse and complement density analyses

For assessing the density of presynaptic inputs (VGluT1, VGluT2) and postsynaptic compartments (Homer1, PSD-95), and for determining the deposition of complement components (C1q, C3), two stained sections from each sample containing the LGN (human and marmoset) or dorsal LGN (mice) were imaged on a Zeiss LSM700 laser scanning confocal microscope equipped with 405 nm, 488 nm, 555 nm, and 639 nm lasers and Zen black acquisition software (Zeiss; Oberkochen, Germany). For each hemisphere, 2-3 randomly chosen 63x fields of view within the LGN were acquired with three z stack steps at 0.68 μm spacing. Identical settings were used to acquire images from all samples within one experiment, and data analyses were performed using ImageJ (NIH, version 1.52k) as described previously with minor modifications (Schafer et al., 2012; Hong et al., 2016a). First, to determine a consistent threshold range, sample images for each genotype and condition were subjected to background subtraction and then manual thresholding blinded to condition and genotype for each channel within one experiment was performed (IsoData segmentation method, 85-255). Then, each channel from single z-planes of the z stacks (3 z-planes per animal) were subjected to the same background subtraction and thresholding, which was kept consistent for a given experiment. Using the analyze particles function, the total area of presynaptic inputs, postsynaptic compartments and complement component deposition was measured from the thresholded images. To quantify the total area of structural synapses, the image calculator tool was first used to visualize colocalized pre- and postsynaptic puncta from the previously thresholded images. Then, the analyze particles function was used to calculate the total area of colocalized signals. Colocalization of complement components (C1q, C3) or Crry-EGFP with presynaptic puncta was performed similarly. Data from single planes was averaged for each z stack of each field of view, and the mean of all fields of view from one animal was determined to calculate densities.

Density analysis of myelin, nodes, paranodes and axons

Similar to the quantification of synapses, densities of myelin (MOG, MAG, MBP), axons (neurofilament, MAP2), as well as nodes of Ranvier (βIV-spectrin) and paranodal junctions (CASPR) were determined. In brief, 2-3 randomly chosen 20x fields of view within the region of interest (ROI; LGN, optic nerve, optic tract) of 2-3 slides per animal were acquired with three z stack steps at 0.44 μm spacing from each animal on a Zeiss Observer Spinning Disk Confocal microscope. Identical settings were used for the acquisition of all images from one experiment, and areas outlining the desired ROI (LGN, retina, optic nerve) were selected and quantified blind to genotype or condition with ImageJ as described above for the synapse analyses.

Cell density quantification

For determining the density of microglia (P2RY12), neurons (NeuN, MAP2, RBPMS, Nissl), infiltrating peripheral immune cells (CD3, CD8, CD45, FoxP3, Ly6C, Clec12a), apoptotic cells (cleaved caspase 3) and degenerating axons (APP), single plane 10x and 20x fluorescence images were collected from both hemispheres of at least two slices from each animal with a Zeiss Observer microscope (Zeiss; Oberkochen, Germany). Identical settings were used for the acquisition of all images from one experiment, and areas outlining the desired ROIs (LGN, retina, optic nerve) were manually counted blind to treatment or genotype using Zen Blue software (Zeiss). The counts were normalized to the total area of the selected ROIs to calculate cell densities.

Fluorescence intensity analysis

For determination of GFAP, P2RY12, Clec7a, and Crry fluorescence intensities in the LGN, 10x and 20x single plane epifluorescence images were collected from both hemispheres of at least two slices from each animal with a Zeiss Observer microscope equipped with Zen Blue software (Zeiss; Oberkochen, Germany). Identical settings were used to acquire images for all samples within one experiment and data analyses were performed using ImageJ (NIH, version 1.52k) and blinded to genotype or conditions of samples. Before quantification, thresholds of pixel intensity were set to the full range of 16-bit images to ensure a consistent pixel range across all images and background was subtracted from all images. To sample fluorescence intensity, ROIs covering either the entire LGN or non-synaptic ($VGluT1^-$ and $VGluT2^-$) and synaptic ($VGluT1^+$ and $VGluT2^+$) areas of the LGN were manually selected for each image and the raw integrated density of pixels within each ROI was measured. Average intensity over all ROIs was quantified for each animal and then normalized to the values of control treated animals.

Microglia soma size determination

For measuring the soma size of microglia, two sections from each sample containing the dorsal LGN were immunostained against P2RY12 and imaged on an Observer Spinning Disk Confocal microscope equipped with diode lasers (405 nm, 488 nm, 594 nm, 647 nm) and Zen Blue acquisition software (Zeiss; Oberkochen, Germany). For each hemisphere, 2-3 randomly chosen 63x fields of view within the LGN were acquired with three z stack steps at 0.68 μm spacing. Manually thresholded maximum projections of the z stacks were generated using ImageJ and microglia soma were outlined using the free hand ROI tool. The microglia soma area was then determined using the analyze measure function.

RNA in situ hybridization

RNA *in situ* hybridization was performed according to the manufacturer's specification (ACDBio; Newark, CA). Briefly, two sections from each sample containing the LGN were treated with "Protease III" for 20 min at 40°C, rinsed with RNase free water and incubated with RNA *in situ* probes against *Il-6* (ACDBio, 315891) or *Il-1*β (ACDBio, 316891) for 2 h at 40°C. Subsequent amplification steps were performed according to the manufacturer's specification. Following *in situ* hybridization, slices were washed in PBS, blocked for 30 min in 2% normal goat serum containing 0.01% Triton X-100, and incubated with rabbit pAb α-P2RY12 (AnaSpec, AS-55043A, 1:2000) overnight at room temperature for immunostaining of microglia. The following day, sections were washed, incubated with the appropriate secondary antibody and mounted with vectashield containing DAPI (Vector laboratories, Burlingame, CA, USA). For each hemisphere, 2-3 randomly chosen 63x fields of view within the LGN were acquired on an Observer Spinning Disk Confocal microscope equipped with diode lasers (405 nm, 488 nm, 594 nm, 647 nm) and Zen Blue acquisition software (Zeiss; Oberkochen, Germany). For quantification, fluorescent RNA signals within $P2RY12^{+}$-microglia were counted manually using ImageJ.

Electron microscopy and G-ratio determination

At the indicated time points, mice were deeply anesthetized and transcardially perfused with 200 mL (10 mL/min) 2% paraformaldehyde and 1% glutaraldehyde (Ted Pella) in 0.12M Millonig's phosphate buffer (pH 7.3). Optic nerves were carefully dissected and post-fixed at 4°C for an additional 4 h in the same fixative. The specimens were then rinsed in Millonig's phosphate buffer, osmicated in 1% osmium tetroxide, dehydrated in ethanol and propylene oxide (Ted Pella), and embedded in Epon plastic resin (Ted Pella). Transverse ultrathin sections of 60-70 nm thickness were collected using an RMC PowerTome ultramicrotome (Boeckeler Instruments) on formvar coated single slot copper grids (Ted Pella), counterstained with uranyl acetate and lead citrate. The sections were analyzed under a transmission electron microscope operating at 80 KV (Tecnai G2 Spirit Twin, FEI, ThermoFisher Scientific). Optic nerves were photographed using a Gatan Orius SC 1000B digital camera (Gatan) at 4,400 x magnification, and the images were used for ultrastructural analysis and G-ratio calculations (G-ratio = axon diameter/fiber diameter).

Generation of adeno-associated viral vector expressing Crry

The pAAV-CB6-PI plasmid (4045 bp) (Gene Therapy Center, UMass Medical School, Worcester, MA, USA) was used as vector backbone in this study. Sequences encoding the complement inhibitor Crry fused to a CR2 sequence and followed by an autocleavage side and the sequence for EGFP were synthesized as two separate gBlock gene fragments (IDT, Skokie, IL). The first gBlock (1382 bp) encoded the sequence for the mature murine Crry protein (residues 1-319, GenBank accession number NM013499) flanked by overhangs (~25bp) with the backbone at the 5′-terminus and the second gBlock at the 3′-terminus (covering parts of the $(G_4S)_2$ linker sequence). The second gBlock (1645 bp) encoded the sequence for a $(G_4S)_2$ linker directly fused to a sequence encoding 4 N-terminal short consensus repeats of a CR2-sequence (residues 1-257 of mature protein, GenBank accession number M35684), followed by the sequence of a porcine teschovirus-1 2A (P2A) autocleavage site and the sequence for EGFP (New England Biolabs, NEBuilder Assembly Tool 2.0.8). At the 3′-terminus, the second gBlock was flanked by an overhang with the backbone and at the 5′-terminus with an overhang (both ~25bp) identical to terminal parts of the Crry sequence of the 3′ end of the first gBlock. Both gBlocks were PCR-amplified, purified and cleaned before sequences were confirmed by Sanger sequencing. To assemble gBlocks with the backbone, the one-step isothermal NEBuilder HiFi DNA assembly cloning method has been utilized according to the manufacture's recommendations (New England Biolabs, Ipswich, MA, #E2621L). 4 μl of the assembly reaction were used for transformation of Stbl3 chemically competent *E. coli* (Thermo Fisher Scientific, #C737303) and bacterial plasmid DNA extraction was performed using QIAfilter Plasmid Mega Kit (QIAGEN, #12281) according to the manufacturer's recommendations. Control constructs encoding the sequence for EGFP but, lacking the sequences for Crry fused to CR2, were generated by restriction enzyme digest (NheI/StyI) and religation of final construct. Restriction analysis of the constructs was performed with the following enzymes or combination of enzymes: SmoI, HincIII, XhoI/XbaI, BamHI, SalI/XhoI, XhoI, BamsHI/EcoRV and HindIII (all from New England Biolabs). The final constructs were further verified by sequencing analysis and subsequently packaged as AAV9 vectors by the UMass Viral Vector Core of the Gene Therapy Center at the University of Massachusetts Medical School.

Intravitreal injection of AAVs

Four-week-old mice were deeply anesthetized with isoflurane, the surrounding tissue around the eye was swabbed with 5% povidone-iodine, and an incision was made into the sclera (app. 2 mm posterior of the superior limbus) using a sterile, sharp 30G needle. After careful removal of the 30G needle, a 33G blunt needle (Hamilton, 1.5"/PT3, #7803-05) attached to a 10 μL gastight syringe (Hamilton, #1701) was carefully inserted into the same incision and viral suspension was injected into the vitreous without damaging the lens or retina. Viral suspension (3 μl) was injected at a titer of 2.5×10^{13} genome copies (GC)/mL. After injection, the needle was

kept inside the vitreous for ~1 min. Mice received injections into both eyes. Finally, ophthalmic antibiotic ointment and local anesthetic were applied. Mice were placed in their home cage on a 37°C heating pad and monitored until they recovered from anesthesia. Twenty-eight days after AAV-injection, EAE was induced in the mice as described above. Only mice that showed substantial colocalization (< 35%) of EGFP with VGluT2$^+$-retinogeniculate terminals in the LGN were included in the analyses.

Culture and treatment of neuro-2a cells

Murine neuro-2a cells (N2a) were purchased from ATCC (#CCL-131) and cultured in DMEM (Thermo Fisher) supplemented with 10% fetal bovine serum (HyClone, USA) and 1% penicillin-streptomycin at 37°C in a humidified incubator. At ~80% confluency, cells were passaged. For AAV-mediated transduction, N2a cells were seeded and, after full attachment to the plate, treated with 25 μM all trans-retinoic acid (RA, Sigma, #R2625) to induce neurite outgrowth. The next day, cells were inoculated with either AAV-Crry or AAV-EGFP with a MOI of 10^5 GC/cell. AAVs were removed 48 h after infection and cells were harvested or fixed for analysis another five days later.

Western blot

Samples were lysed in T-PER (Thermo Scientific), boiled at 95°C for 10 min, separated on 4%–20% Mini-PROTEAN TGX Gels under reducing conditions, and transferred to polyvinylidene diflouride membrane. After blocking with 5% (w/v) non-fat milk/PBS (all from BioRad), membranes were incubated with the following antibodies: mouse mAb α-Crry (clone TLD-1C11, Santa Cruz, sc-53530, 1:100), rabbit pAb α-EGFP (Millipore, ab3080P, 1:1000), goat pAb α-GAPDH (Abcam, ab9483, 1:1000), and respective peroxidase-conjugated secondary antibodies (BioRad). Signals were visualized by enhanced chemiluminescence. Prior to the detection of further antigens on the same membrane, antibodies were washed off with Restore Plus Western Blot Stripping Buffer (Thermo Scientific).

Optomotor testing

Assessment of visual acuity was performed before the induction of EAE and at the onset of clinical symptoms in awake, freely moving mice. Individual mice were placed on a round, elevated platform in the center of a soundproof chamber that was surrounded by four computer screens on which visual stimuli were projected. Mice were exposed to a virtual cylinder consisting of rotating sine wave gratings (12 deg/s) of various spatial frequencies (cycles/degree). Mice reflexively track these gratings by stereotypic head movements as long as the grating is visible (Prusky et al., 2004). To determine grating acuity, first a homogeneous gray stimulus was projected on the cylinder, which was followed by a low-spatial-frequency (0.05 cyc/deg) sine wave grating of the same mean luminance that was randomly rotating in one horizontal direction. A video camera positioned in the lid of the chamber directly above the animal was used by a trained observer to record the mice and assess smooth, reflexive head movements in response to the rotating gratings. To determine the highest spatial frequency perceptible for each individual mouse, the spatial frequency of the grating was systematically increased until the animal no longer responded to the projected grating. Visual acuity was assessed blind to treatment of animals.

QUANTIFICATION AND STATISTICAL ANALYSIS

Results are expressed as means ± standard error (SEM) from at least three independent replicates for each experimental group. Two-tailed Student's t test to compare two groups or one-way analysis of variance (ANOVA) followed by Tukey's multiple comparison post hoc test to compare multiple groups was performed using Prism 7 software (Graph-Pad, La Jolla, CA, USA). Values of $^*p < 0.05$, $^{**}p < 0.01$, $^{***}p < 0.001$, $^{****}p < 0.0001$ were considered statistically significant.

DATA AND CODE AVAILABILITY

This study did not generate any unique datasets or code.